REPORT DOCUMENTATION PAGE

1. REPORT DATE (DD-MM-YYYY)	2. REPORT TYPE	3. DATES COVERED (From - To)
October 2012	Journal Article	October 2012- December 2012

4. TITLE AND SUBTITLE

Microstructure Statistics Property Relations of Anisotropic Polydisperse Particulate Composites using Tomography

5a. CONTRACT NUMBER
In-House

5b. GRANT NUMBER

5c. PROGRAM ELEMENT NUMBER

6. AUTHOR(S)

A. Gillman, K. Matous, S. Atkinson

5d. PROJECT NUMBER

5e. TASK NUMBER

5f. WORK UNIT NUMBER
Q0AL

7. PERFORMING ORGANIZATION NAME(S) AND ADDRESS(ES)

Air Force Research Laboratory (AFMC)
AFRL/RQRM
4 Draco Drive.
Edwards AFB CA 93524-7160

8. PERFORMING ORGANIZATION REPORT NO.

9. SPONSORING / MONITORING AGENCY NAME(S) AND ADDRESS(ES)
Air Force Research Laboratory (AFMC)
AFRL/RQR
5 Pollux Drive
Edwards AFB CA 93524-7048

10. SPONSOR/MONITOR'S ACRONYM(S)

11. SPONSOR/MONITOR'S REPORT NUMBER(S)

AFRL-RQ-ED-JA-2012-362

12. DISTRIBUTION / AVAILABILITY STATEMENT
Distribution A: Approved for Public Release; Distribution Unlimited. PA#12905

13. SUPPLEMENTARY NOTES

14. ABSTRACT
In this paper, a systematic method is presented for developing microstructure-statistics-property relations of anisotropic polydisperse particulate composites using micro-computer tomography (micro-CT). Micro-CT is used to obtain a detailed three-dimensional representation of the polydisperse microstructures, and a novel image processing pipeline is developed for identifying particles. In this work, particles are modeled as idealized shapes in order to guide the image processing steps and to provide a description of the discrete micro-CT dataset in continuous Euclidean space. N-point probability functions used to describe the morphology of the mixtures are calculated directly from real microstructures. The statistical descriptors are employed in the Hashin-Shtrikman variational principle to compute overall anisotropic bounds and self-consistent estimates of the thermal conductivity tensor. We make no assumptions of statistical isotropy nor ellipsoidal symmetry, and the microstructural description is obtained directly from micro-CT data. Various mixtures consisting of polydisperse ellipsoidal and spherical particles are prepared and studied to show how the morphology impacts the overall anisotropic thermal conductivity tensor.

15. SUBJECT TERMS

16. SECURITY CLASSIFICATION OF:			17. LIMITATION OF ABSTRACT	18. NUMBER OF PAGES	19a. NAME OF RESPONSIBLE PERSON William Harrigan
a. REPORT Unclassified	**b. ABSTRACT** Unclassified	**c. THIS PAGE** Unclassified	SAR	44	**19b. TELEPHONE NO** (include area code) 661-525-5328

Microstructure Statistics Property Relations of Anisotropic Polydisperse Particulate Composites using Tomography[*]

A. Gillman, K. Matouš,[†] and S. Atkinson

Department of Aerospace and Mechanical Engineering

University of Notre Dame, Notre Dame, IN, 46556, USA

(Dated: October 9, 2012)

Abstract

In this paper, a systematic method is presented for developing microstructure-statistics-property relations of anisotropic polydisperse particulate composites using micro-computer tomography (micro-CT). Micro-CT is used to obtain a detailed three-dimensional representation of the polydisperse microstructures, and a novel image processing pipeline is developed for identifying particles. In this work, particles are modeled as idealized shapes in order to guide the image processing steps and to provide a description of the discrete micro-CT dataset in continuous Euclidean space. n-point probability functions used to describe the morphology of the mixtures are calculated directly from real microstructures. The statistical descriptors are employed in the Hashin-Shtrikman variational principle to compute overall anisotropic bounds and self-consistent estimates of the thermal conductivity tensor. We make no assumptions of statistical isotropy nor ellipsoidal symmetry, and the microstructural description is obtained directly from micro-CT data. Various mixtures consisting of polydisperse ellipsoidal and spherical particles are prepared and studied to show how the morphology impacts the overall anisotropic thermal conductivity tensor.

PACS numbers: 45.70.-n,05.20.-y,46.65.+g,87.59.-e

I. INTRODUCTION

Accurately characterizing particulate mixtures is critical to a variety of scientific fields including heterogeneous materials like solid rocket propellants [1, 2], granular materials like sand [3], low-temperature phases of matter [4], and biological applications such as protein configurations [5]. Processing plays a critical role in material science also. It is known that material manufacturing steps lead to anisotropic morphologies. For example, in solid propellants an uneven burning profile is observed due to particle alignment across the propellant grain, which is attributed to the casting procedure [6]. Moreover, determining optimal packings of various shapes is a fundamental mathematical problem that has been studied for centuries [7, 8]. Often, packing algorithms are used to study how particles arrange and are the basis for analyzing the effect of the morphology on physical phenomena [9–11]. However, Caulkin et al. [12] showed that one must consider physical interaction forces due to material formulation steps in these algorithms to model real microstructures accurately. This is a difficult task computationally. Therefore, micro-computer tomography (micro-CT) has become a popular method for obtaining a description of real microstructures including solid propellants [13, 14], glass beads [15, 16], and Fontainebleau sandstone [17], just to name a few. Moreover, tomography characterization methods can be used to validate packing algorithms.

For analyzing various material systems, statistical characterization methods have been used to describe these complicated microstructures. Bernal [18] motivated the importance of higher-order statistics using the radial distribution function to describe the structures of liquids. Frisch and Stillinger [19] introduced n-point probability functions to describe radiation scattering in packs of monodisperse spheres. Note that n-point probability functions can be used to statistically characterize a general class of microstructures including porous materials and particulate packs of arbitrarily shaped inclusions. The significance of the statistical description has also been shown in several other fields of physics including condensed matter physics with applications to disordered materials through non-Gaussian noise [20] and to cosmic radiation using Minkowski functionals [21]. While these statistical descriptors have been used for decades, accurately obtaining higher order statistical information of real systems in three dimensions has proved difficult to this day. Coker and Torquato [22] and Yeong and Torquato [23] computed two-point probabilities functions of a

2

two-phase material, yet considered only two-dimensional slices and assumed rotational and translational invariance of the functions. Fullwood et al. [24] computed n-point probability functions of three-dimensional two-phase materials, but their computations were limited to relatively small systems. In [15, 25], radial distribution functions are used to statistically characterize the microstructures, which are limited to packs of spheres. As multi-phase polydisperse systems are considered in three dimensions, large packs must be used, resulting in even larger datasets. In our prior work [16], one-, two-, and three-point probability functions were calculated for a three-dimensional system of polydisperse spheres from micro-CT data. Mecke and Arns [26] alternatively used Minkowski functionals as statistical descriptors to describe porous materials, such as soils and sedimentary rocks. The Minkowski functionals are better suited for two-phase materials characterized by a Boolean model in which a material skeleton is represented with overlapping inclusions.

Linking the morphology to the overall material response is a longstanding problem. The seminal multiscale techniques proposed by Hashin and Shtrikman [27], Willis [28], Bensoussan et al. [29], Hill [30], and Torquato [31] deserve attention, and many others have also contributed [32–35]. As computationally and tomographically derived packs are often too large for practical numerical simulations of nonlinear processes [1, 36], work has been dedicated to reconstructing statistically equivalent unit cells [16, 37]. In contrast to numerical simulations [1, 36], analytical and semi-analytical techniques are an alternative means of computing the overall response of heterogeneous materials. The work of Willis is of particular importance as it established a direct link between the statistical description and properties [28]. However, in [28] results were only obtained for simple morphologies with statistically isotropic or ellipsoidal symmetric statistics. This limitation is due to challenges in integrating complex integral kernels that are products of the second derivative of Green's function and two-point probability functions. Drugan and Willis [38], when formulating a non-local model, were limited to obtaining overall properties for two-phase systems with an isotropic distribution of monomodal spheres. In the work of Torquato and Sen [39], only statistically isotropic microstructures and those composed of aligned arbitrarily shaped inclusions were discussed. Ponte Castaneda [40] among others [38, 41] have proposed a third order model for nonlinear materials, yet once again only simple microstructures were considered due to the difficulty in obtaining real probability functions and integrating over them.

In this work, voxel datsets consisting of polydisperse particles of multiple shapes are studied. Using our SHAPE3D software package, particles in a voxel dataset are modeled as ellipsoids by minimizing differences in geometric quantities between the voxel and Euclidean, $\mathbb{R}^3$, representations. This description in continuous Euclidean space can simplify analysis of such systems, improve their understanding, and aid in the development of new material formulations. Moreover, an idealized mapping can reduce the size of the dataset. This reduction becomes increasingly important as more complicated systems are studied, and larger voxel datasets must be considered in order to resolve all important morphological features. Note that state of the art in micro-CT analysis of highly packed particulate systems has been limited, to the best of our knowledge, to nearly monodisperse packs [12, 15, 25], and these works do not discuss in detail image processing steps. However, image processing steps can pollute mechanical and transport properties predictions that are obtained from improperly segmented/processed images. When considering polydisperse packs of various inclusions, a traditional image processing pipeline does not properly identify individual particles. Thus, a novel image processing pipeline is presented.

Next, we compute overall anisotropic properties without traditional assumptions on the complexity of the microstructure (statistically isotropic, aligned inclusions). We show that for systems of polydisperse unaligned inclusions, the importance of eliminating these assumptions is critical. The n-point probability functions are computed directly from three-dimensional micro-CT datasets using our code, STAT3D [16]. We consider polydisperse systems and present that statistical functions are not isotropic nor possess ellipsoidal or any other material symmetry. Thus, the closed-form solutions of overall properties are unachievable. Therefore, based on our prior work [42], the complex integrals containing the n-point probability functions and the second derivative of the Green's function are computed numerically. Various compositions of polydisperse mixtures of spheres and ellipsoids are considered, and overall anisotropic thermal conductivity tensors are predicted.

II.   SAMPLE PREPARATION, MICRO-CT SCANNING, AND PARTICLE CHARACTERIZATION

This section describes the methods to mix and pack polydisperse systems, to acquire data using micro-CT, to process datasets using image processing algorithms, and to model

particles as ideal shapes. In this work, a surrogate system of rice grains and mustard seeds is used for their ellipsoidal and spherical shape, respectively. In our discussion, we label the mustard seeds as spheres due to their low eccentricities. However, all particles are modeled as ellipsoids.

A. Packing of Polydisperse Particulate Mixtures

Two packing methods were developed with previous studies in mind [15, 43, 44]. The first method is used for packing homogeneous polydisperse mixtures of ellipsoids and spheres while limiting boundary effects. Packs mixed using this method will be referred to as randomized packs. The second method is used for packing ordered systems of particles, with the goal of obtaining aligned inclusions. Packs created with aligned particles are referred to as semi-ordered packs.

FIG. 1. The scanning container filled with 50% weight of spheres to ellipsoids. Note the hemispherical beads on the boundary of the container used to minimize boundary effects.

First, the preparation of randomized packs of polydisperse systems is described. The container, as seen in Figure 1, was designed to eliminate boundary effects and fill the entire viewing area within the micro-CT scanner. The container has a diameter of 62 mm and height of 65 mm, and hemispherical beads (3 mm radius) are attached to the boundary in order to minimize boundary effects. The randomized packs are prepared in the following steps: *I*) Amount of each constituent (e.g. spheres, ellipsoids, etc.) is weighed with a high

precision scale with 0.001 g accuracy. *II*) Constituents are mixed together in a large bowl. *III*) Mixture is poured into scanning container. *IV*) Scanning container is shaken in all directions. *V*) Container is tapped allowing particles to settle and reach maximum volume fraction. Let us note that steps *II* and *IV* are repeated until the mixtures are visually homogeneous.

To prepare semi-ordered packs of aligned particles, a separate sample preparation strategy is used. The same sized cylindrical container was used, but no hemispherical beads were attached to the boundary of the container in order to prevent the irregular boundary from randomizing the sample. The semi-ordered packs are prepared in the following steps: *I*) A thin layer of particles is poured into container. *II*) On a flat surface, container is oscillated back and forth twenty times in the same direction. *III*) Tap container five times. These steps are applied to thin layers so that the particles on top of the pack can move freely. We repeat these steps until the container is full. The oscillation in the same direction allows particles to align, and the tapping is again done to reach a maximum volume fraction.

B. Dataset Acquisition

Once the packs are prepared, all samples are scanned using a Skyscan 1172 micro-CT machine. This particular scanner has the ability to produce datasets that capture features that are ~ 0.7 μm. A convergence study was done on a pack of polydisperse spheres to show that the particle volume fraction of a sample is maintained for resolutions of 69.4, 34.7, 17.4, and 8.7 μm per pixel. The standard deviation in volume fraction for all of these scans was 0.0055, which is less than 1% of the mean volume fraction. A resolution of 69.4 μm per pixel was selected for all compositions described in this work. All datasets are on the order of 10^8 voxels (voxel = 3D pixel). The average diameter of the spherical particles, the smallest sized inclusion in our mixtures, is ~ 2 mm. With a resolution of 69.4 μm, this is $\sim$30 voxels in diameter, which is a good resolution for the statistical characterization that follows.

The three-dimensional voxel dataset of the 50% weight fraction of spherical to ellipsoidal particles is shown in Figure 2. This dataset will be used to describe steps for characterizeing the microstructure. This cylindrical dataset has a diameter of $D = 57.67$ mm (831 pixels) and a height of $H = 48.51$ mm (699 pixels), which corresponds to 3.79×10^8 voxels.
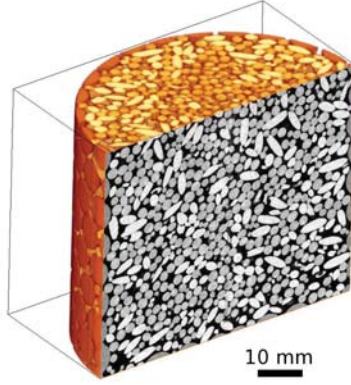
6

FIG. 2. The surrogate system of ellipsoids and spheres with 50% weight fraction of constituents. Observe the hemispherical beads at the boundary that are used to randomize the packs and limit boundary effects. The brightest particles correspond to the ellipsoidal particles, while the darker ones correspond to spherical ones.

C. Image Processing

Once the three-dimensional voxel dataset is obtained, image processing algorithms are used to identify particles, and these voxel particles are then modeled as idealized shapes. The purpose of characterizing particles as idealized shapes is to understand the influence of different particle types on the macroscopic behavior and to provide a description of the microstructure in continuous Euclidean space, $\mathbb{R}^3$. This compact representation can be beneficial for design of new material formulations, for example. Image processing routines for identifying particles in a voxel dataset are well established [45]. For a system of monodisperse, convex-shaped objects with no hollow regions, a typical image processing pipeline is to eliminate noise in the dataset by using an edge-preserving smoothing algorithm, to identify the particulate material by thresholding, and to segment the dataset such that individual particles are represented by connected groups of voxels. Two common segmentation algorithms are watershed-based segmentation and the opening algorithm (erosion followed by dilation). Unfortunately, a watershed-based algorithm is limited as it only properly separates datasets of mono-disperse convex-shaped objects, while the opening algorithm distorts shapes for non-spherical objects. In general, all segmentation algorithms lead to some volume removal. For polydisperse systems with non-convex features, these standard image processing steps will result in improperly segmented datasets [45]. As real materials consist

7

of irregularities, such as voids, non-convex surfaces, varying densities, etc., this traditional processing pipeline must be enhanced to accurately capture real microstructures.
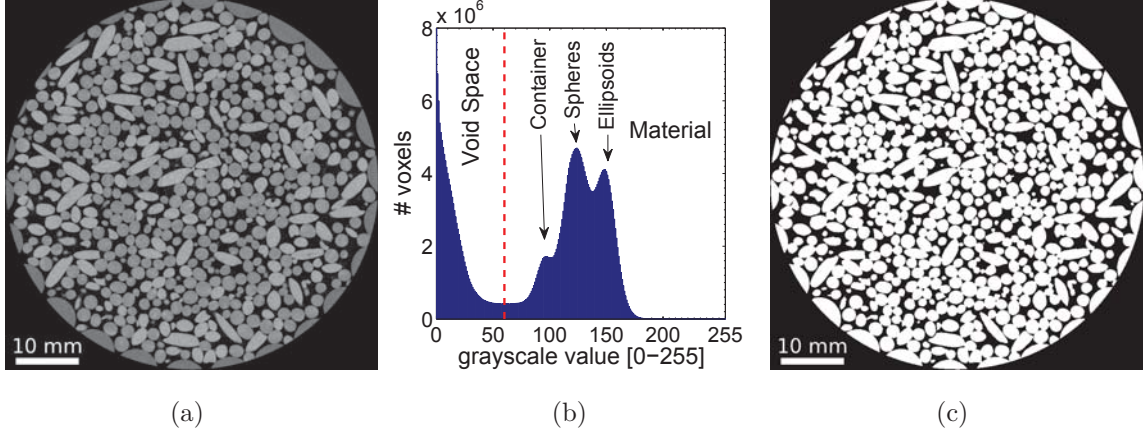

FIG. 3. Illustration of image processing steps *i-iii*.

In order to limit and control the errors in the image processing pipeline, we propose a novel strategy based on interplay between voxel analysis and analysis in $\mathbb{R}^3$. The following image processing steps were developed using Visage Imaging Inc.'s *Amira* [46] in conjunction with Skyscan's *CTAn* [47] and the SHAPE3D software developed in this work: *i*) The voxel dataset is smoothed using the Kuwahara edge-preserving median filter algorithm [48] in order to eliminate noise. A resulting two-dimensional slice of the dataset after smoothing is presented in Figure 3(a). *ii*) The particulate phases are thresholded based on the grayscale distribution of particles (Figure 3(b)). In this distribution, the three peaks on the right are related to the average grayscale values of the ellipsoids, spheres, and the container and the left peak is considered void space. The threshold cutoff (red dashed line), which distinguishes between void space and material, is chosen to be the local minimum value between the two leftmost peaks and is 60 for this dataset. *iii*) Voids within the particles are filled. The resulting dataset slice after this step is presented in Figure 3(c). Notice how many of these particles are joined. *iv*) A watershed segmentation algorithm is used to separate individual particles. *v*) To eliminate the boundary effects due to the hemispherical beads that are fixed to the scanning container, a volume of interest (VOI) is defined. The VOI (the circular blue region in Figure 4(a)) is chosen such that the boundary effects on the statistical characteristics are minimized/eliminated. The VOI is determined by decreasing the cylindrical volume's diameter and height by increments of 10 voxels until the particle

volume fraction saturates to within 1%. The resulting VOI has a diameter of $D_{\text{VOI}} = 46.57$ mm and a height of $H_{\text{VOI}} = 37.4$ mm (63.70 cm^3). vi) Geometric quantities of individual particles including volume, surface area, moments of inertia, the mean grayscale value and centroid coordinates are computed. vii) It is determined which particles are still
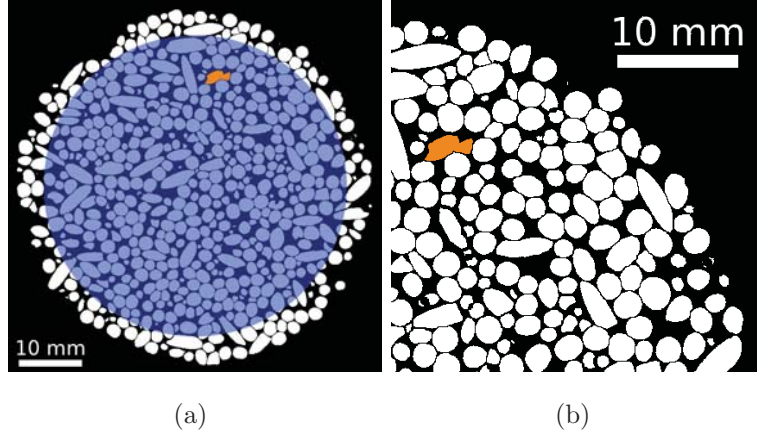

(a) (b)

FIG. 4. Illustration of image processing steps iv-vii. (a) A dataset slice after image segmentation in step iv. (b) A section of (a) that illustrates particles remaining connected after step vi (highlighted in orange).

connected due to the inefficiency of the segmentation algorithm, and these particles are marked (Figure 4(b)). To determine which particles were not separated in step iv, one can analyze certain geometric quantities of the voxel particles to see if they match the parameters of the shapes expected in the sample, i.e. if some voxel particles are larger than the known distribution of particles, they should be segmented further. Because this system is composed of particles closely resembling ellipsoids, a voxel particle not matching an ellipsoid is marked for additional image segmentation steps. The method for modeling a voxel particle as an ellipsoid using our SHAPE3D package is described in subsection II D. $viii$) A combination of the opening algorithm with watershed segmentation is used to separate the marked particles identified in step vii using SHAPE3D (see subsection II D). ix) For newly separated particles, geometric quantities are computed. x) The phase of each particle is determined based on the mean grayscale value. The average grayscale value of each particle is described in Figures 5(b) and 5(c), where d is the representative sphere diameter. Considering the local minimum in Figure 5(b) and the distribution of particle sizes in Figure 5(c), the average grayscale cutoff value for the 50% weight fraction of spheres is 136.
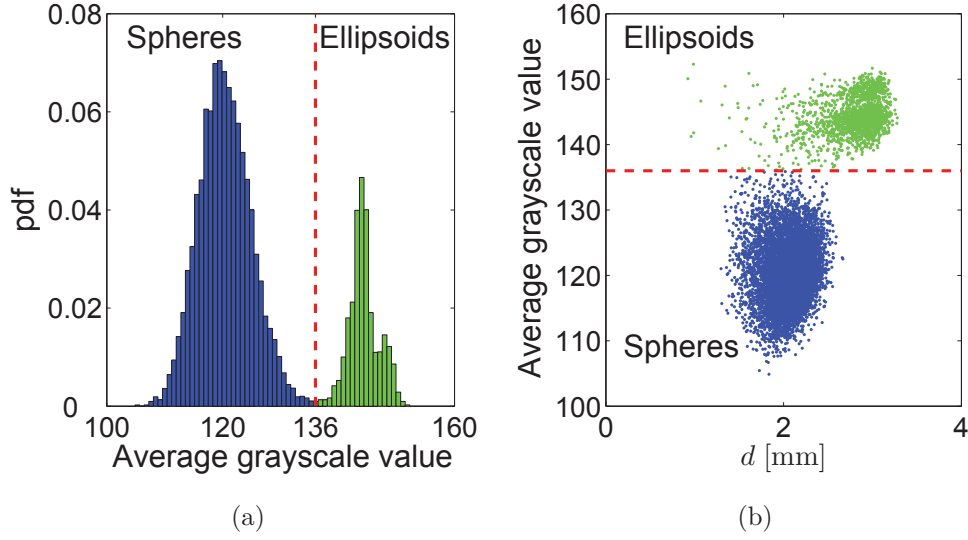
9

FIG. 5. Illustration of image processing step x.

Figure 6 shows the resulting dataset after image processing, where the spherical and ellipsoidal particles are colored blue and green, respectively. Packs of voxel particles will be referred to as the voxel packs. An error measure is introduced to quantify the volume loss due to the image segmentation steps,

$$0 \leq \varepsilon_{IP} = \frac{|c_p^{v,B} - c_p^{v,A}|}{c_p^{v,B}} \times 100 \leq 100 \ [\%], \tag{1}$$

where $c_p^{v,B}$ and $c_p^{v,A}$ are the total particle volume fractions of the voxel pack before and after image segmentation steps, respectively. For the 50% weight spherical particle pack, $c_p^{v,B} = 0.6770$ and $c_p^{v,A} = 0.6594$, which represents a volume loss of $\varepsilon_{IP} = 2.60\%$ as a result of the image segmentation algorithms used. Note that the respective phases (mustard and rice) can only be identified after all image segmentation steps, and c_e^v and c_s^v will refer to the volume fractions of ellipsoids and spheres in the voxel pack ($c_p^{v,A} = c_e^v + c_s^v$), respectively. For this pack, $c_e^v = 0.2701$ and $c_s^v = 0.3893$. Relevant information including the volume fractions and other morphological characteristics of all mixtures studied are presented at the end of this section (see Tables I and II).

D. Modeling Voxel Pack as Pack of Idealized Shapes

Taking into consideration knowledge about the microstructure, all voxel particles are modeled as ellipsoids in $\mathbb{R}^3$. The voxel particles are fitted to idealized shapes by optimizing
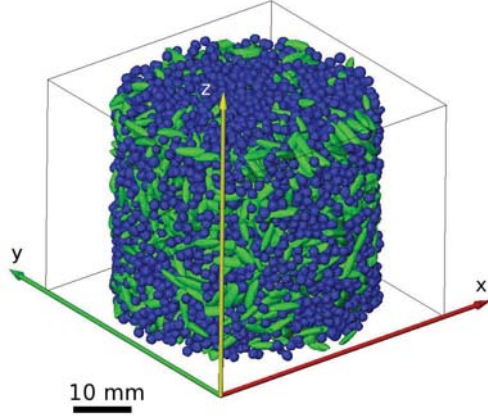
10

FIG. 6. Voxel pack of 50% weight of constituent mixture. The voxel pack is the voxel dataset after image processing.

two fitness functions that best characterize a particle's volume, surface area, and orientation. The first function minimized is

$$\Pi_1(k) = \omega \frac{|k^3 V_{pa} - V_{ct}|}{|V_{ct}|} + (1 - \omega) \frac{|k^2 S_{pa} - S_{ct}|}{|S_{ct}|}, \tag{2}$$

where V_{ct} and S_{ct} are the volume and surface area calculated for a particle in the voxel pack, V_{pa} and S_{pa} are the volume and surface area of the ideal shape being optimized, and ω is a weight factor between a particle's volume to surface area. The weight factor was chosen to be $\omega = 0.8$ in our work. The scaling factor k determines the scale of the final semiaxes as

$$\begin{pmatrix} a \\ b \\ c \end{pmatrix} = k \begin{pmatrix} a^* \\ b^* \\ c^* \end{pmatrix}, \tag{3}$$

where a, b, and c are the final semiaxes of the ideal shape with $a > b > c$. The semiaxes a^*, b^*, and c^* are computed from the inertia tensor of the voxel particle, $\boldsymbol{I}_{ct}$, assuming that the particle is an ellipsoid. The use of a scaling factor k ensures that the ratios between a^*, b^*, and c^* and a, b, and c are preserved so that the idealized particle better mimics the overall shape.

A second fitness function, $\Pi_2(\alpha, \beta, \gamma)$, is defined to adjust the orientation of the idealized shape to best mimic the voxel particle as

$$\Pi_2(\alpha, \beta, \gamma) = \frac{\left|\left| \boldsymbol{R}(\alpha, \beta, \gamma) \boldsymbol{I}_{pa} \boldsymbol{R}(\alpha, \beta, \gamma)^{-1} - \boldsymbol{I}_{ct} \right|\right|_{\mathbb{F}}}{||\boldsymbol{I}_{ct}||_{\mathbb{F}}}, \tag{4}$$

where $\boldsymbol{I}_{pa}$ is the inertia tensor of the ideal shape that is being optimized. α, β, and γ are angles by which the orthogonal rotation matrix $\mathbf{R}$ adjusts $\boldsymbol{I}_{pa}$. Also, $\boldsymbol{A} = \boldsymbol{R}\boldsymbol{A}^*\boldsymbol{R}^{-1} = \left[\boldsymbol{\eta}_1, \boldsymbol{\eta}_2, \boldsymbol{\eta}_3\right]^T$ gives the final orientation vectors $\boldsymbol{\eta}_1$, $\boldsymbol{\eta}_2$, and $\boldsymbol{\eta}_3$ that correspond to the directions of a, b, and c, respectively. Here, $||\bullet||_{\mathbb{F}}$ represents the Frobenius norm. Note that we place the ellipsoid's origin at the centroid (X_c, Y_c, Z_c) of the voxel object, and the density of all particles is assumed constant.

The resulting differences between the voxel and ideal particles are considered by looking at the differences in the volume, surface area, and inertia tensors after optimizing the objective functions. The first metric, ΔV, quantifies the difference in volume (as a percentage) between a voxel particle and its corresponding ellipsoid:

$$0 \leq \Delta V = \frac{|V_{pa} - V_{ct}|}{|V_{ct}|} \times 100 \leq 100 \ [\%]. \tag{5}$$

The second metric, ΔS quantifies the difference in surface area (as a percentage) in the same manner as ΔV (see Equation (5)). The third metric, $\Delta\Pi_2 = \Pi_2 \times 100 \ [\%]$, quantifies differences in orientation. Particles with $\Delta\Pi_2 > 5\%$ are marked in step *vii* for additional segmentation in step *viii* (see orange particle in Figure 4 and description in subsection II C).

The corresponding idealized pack and the distribution of particles for the voxel pack are presented in Figure 7, where e is a measure of eccentricity defined as

$$e = \frac{1}{3}\left(\frac{\sqrt{a^{*2} - b^{*2}}}{a^*} + \frac{\sqrt{b^{*2} - c^{*2}}}{b^*} + \frac{\sqrt{a^{2*} - c^{*2}}}{a^*}\right). \tag{6}$$

Higher values of e correspond to more eccentric particles, and a perfect sphere corresponds to $e = 0$. The distribution outlined in black corresponds to the spheres (blue particles), while the distribution outlined in gray corresponds to ellipsoids (green particles). As can be seen in Figure 7, the average eccentricity of the mustard seeds is small. Thus, they are referred to as spherical. Note that a substantial reduction of the dataset size from $\sim 3.79 \times 10^8$ voxel to 10,620 ellipsoids was achieved. Considering that an ellipsoid is described by the centroid (X_c, Y_c, Z_c), the semiaxes (a, b, c), and three angles $(\alpha, \beta, \text{ and } \gamma)$, we need 9 numbers to characterize an ellipsoidal particle. Thus, 95,580 numbers are needed to describe this pack. Compared to the 3.79×10^8 voxels, this dataset is compressed by approximately four thousand times.

The distributions of the errors in volume, surface area, and inertia tensor for all particles in the pack are shown in Figure 8. All average errors are below 3%. Note that the maximum
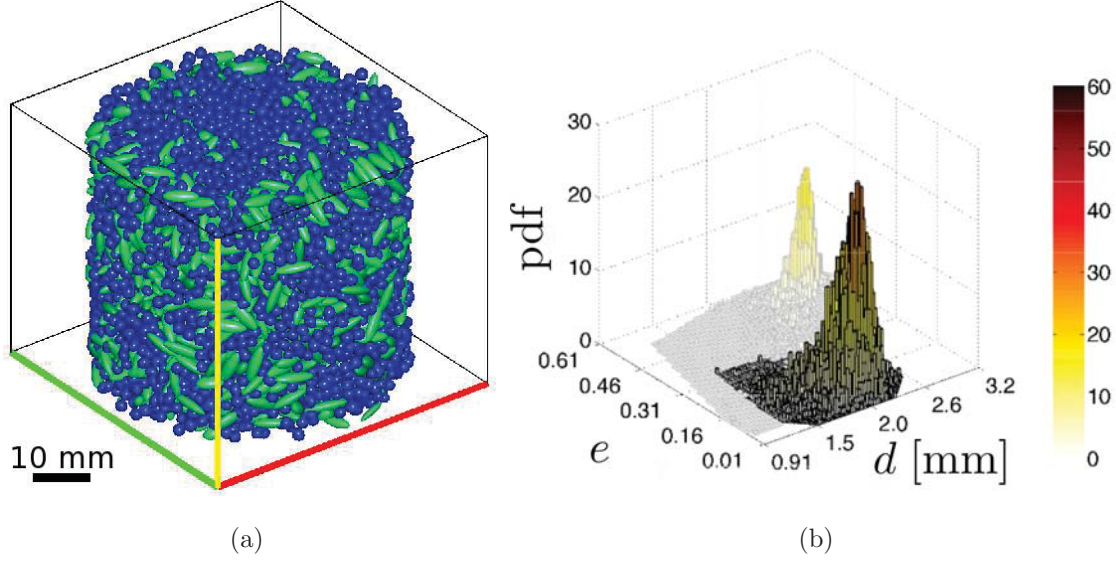
12

FIG. 7. Idealized pack and particle distribution of voxel pack from Figure 6. There are 2276 ellipsoidal and 8344 spherical particles in this pack. Compare (a) to Figure 6.

error in surface area, ΔS, is large relative to ΔV, because the weight factor, ω, favors matching the volume of the particle over the surface area. It is well known that voxel representation of a surface is inaccurate and cannot be improved by increasing the voxel resolution [49]. Capturing the surface area of a voxel object accurately is nontrivial and requires fitting a smooth surface to a stepwise boundary [49, 50]. Because a sophisticated surface representation was not considered in this work, ω was chosen to be 0.8. Nevertheless, only 3.99% of the particles in this pack have $\Delta S > 5\%$. In addition, note that while Π_2 is used to optimize the orientation of the idealized shape, this value is also a measure of how well the idealized shape fits the voxel particle in an overall sense. For this pack, only 0.03% of particles have orientation errors of $\Delta\Pi_2 > 5\%$. Note that using a traditional watershed-based segmentation algorithm without our $\mathbb{R}^3$ mapping (system before step vii) would result in $\Delta\Pi_2(max) = 16.04\%$, and 0.34% of particles having $\Delta\Pi_2 > 5\%$. This shows that a substantial improvement was achieved ($\Delta\Pi_2(max)$ was improved 2× and $\Delta\Pi_2 > 5\%$ was improved 10×).

E. Pack Analysis

Using the microstructure characterization procedures described above, five randomized compositions and one semi-ordered pack of ellipsoids are characterized. These datasets
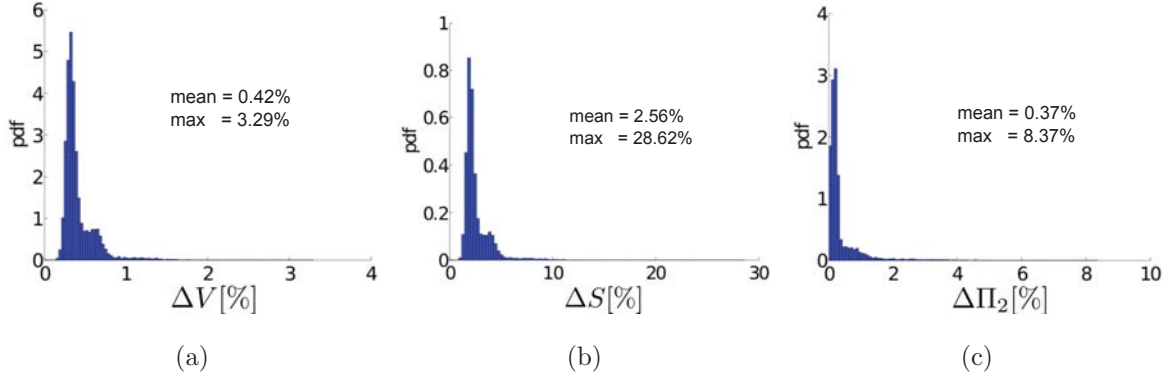
FIG. 8. (a), (b), and (c) are the distributions of particle errors in volume, surface area, and inertia tensors between the voxel and idealized packs, respectively.

provide a foundational dataset for analyzing the microstructure's effect on overall material properties that will be presented in section V.

1. Semi-ordered Pack of Ellipsoids
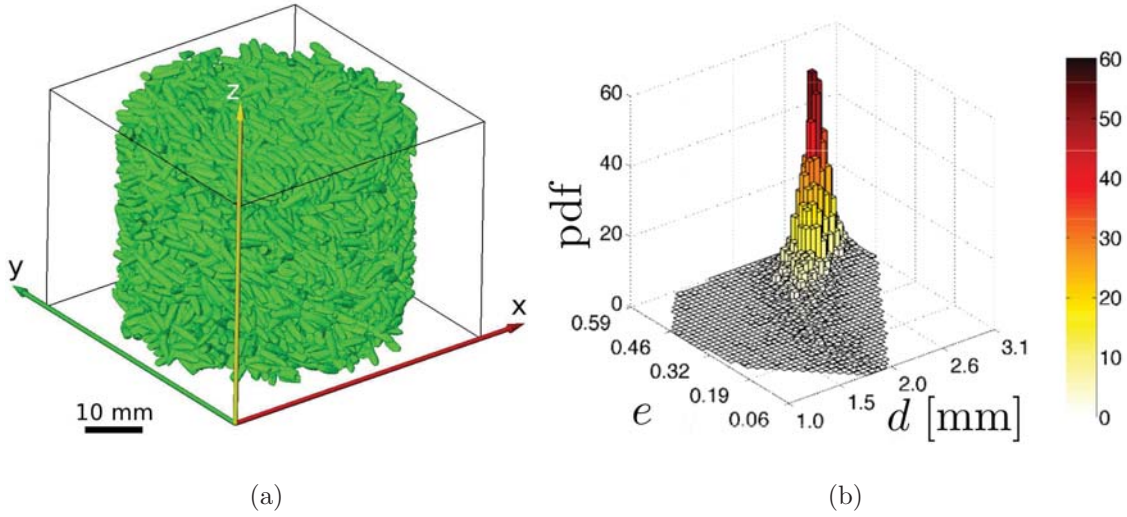
FIG. 9. Voxel pack of semi-ordered ellipsoids. There are 6536 ellipsoidal particles in this pack.

The voxel pack representation after image processing with the associated distribution of particles is presented in Figure 9, where the size of the cylindrical domain analyzed has a diameter of $D = 59.44$ mm and a height of $H = 47.16$ mm. This pack had a particle volume fraction of $c_p^{v,B} = 0.6841$ before particle segmentation and was reduced to $c_p^{v,A} = 0.6655$ after image segmentation steps, corresponding to a volume loss of $\varepsilon_{IP} = 2.71\%$. The VOI for this

sample is $D_{\text{VOI}} = 45.24$ mm and $H_{\text{VOI}} = 33.03$ mm. When modeling the voxel particles as idealized ellipsoids, the mean errors of ΔV, ΔS and $\Delta \Pi_2$ are 0.70%, 4.48%, and 2.20%, respectively. The maximum errors in ΔV, ΔS and $\Delta \Pi_2$ are 2.69%, 20.98%, and 11.65%, and 24.91% and 0.69% of all particles have $\Delta S > 5\%$ and $\Delta \Pi_2 > 5\%$.

In Figure 9(a), it can be seen that the particles are aligned in the y-direction. The orientation of an ellipsoidal particle is described by two angles with respect to the basis vector of the longest semi-axis $\boldsymbol{\eta}_1$: the azimuthal angle (projected orientation onto the xy plane) and the altitude angle (with respect to the z axis). These angles are referred to as θ_a and ϕ_a (see Figure 10) and are found from the orientation of an idealized shape. The distributions of the azimuthal and altitude angles for the semi-ordered pack is presented in Figure 11. The distribution of ϕ_a shows that the ellipsoids are more likely to lie horizontally ($\phi_a = 0°$) than in the unstable vertical position ($\phi_a = 90°$), while the distribution of θ_a shows that the ellipsoids are preferably aligned in the y-direction ($\theta_a = -90° = 90°$), which can also be observed in Figure 9(a). This anisotropic morphology will have a critical impact on the overall thermal conductivity estimates presented in section V.
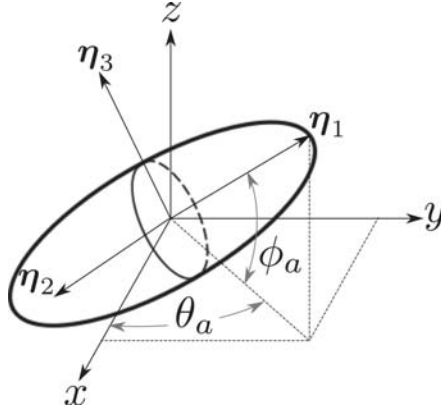
FIG. 10. Definition of ellipsoid's orientation with respect to the largest semiaxis.

2. Randomized Mixtures

Five compositions at 0%, 25%, 50%, 75% and 100% weight of spheres to ellipsoids are considered. These five compositions are created by weighing the appropriate amount of each constituent and are then packed and tomographically characterized two times to confirm the repeatability of the steps described in this section (We refer to these two scans as higher

FIG. 11. Distribution of particle orientations for semi-ordered pack shown in Figure 9(a).

and lower volume fraction packs depending on their packing density). Table I shows information about each voxel pack considered including the weight of each constituent, sizes of the datasets, and the error introduced due to the image segmentation steps. The largest volume losses, ε_{IP}, occur for the spherical particle packs. However, all volume losses are less than 3.66%. Note that the height of the volume analyzed, H, increases with increasing weight % of spherical particles, because the spherical particles are less dense than the ellipsoidal ones. This can be also observed in Figure 2, since darker gray corresponds to less dense material. The resulting volume fractions of all randomized compositions considered in this work before and after image segmentation, $c_p^{v,B}$ and $c_p^{v,A}$, are presented in Figure 12(a). Figure 12(b) shows the volume fraction of each constituent for the corresponding composition. In these figures, the two samples for each composition are represented by the two data points, and the lines are the means. All differences in the total particle volume fractions after segmentation, between the two packs of each composition analy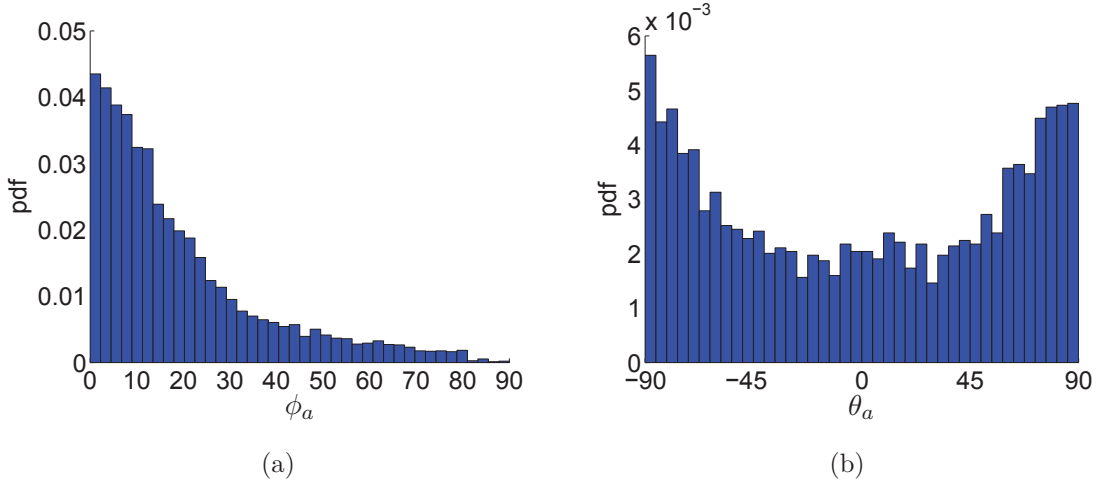zed (higher and lower volume fraction packs), are below 0.008 (maximum difference is for 25% mixture, see Figure 12(a)). The maximum differences between the phase volume fractions, c_e^v and c_s^v, are 0.0191 and 0.0156, respectively, for the 50% mixture (see Figure 12(b)). Recall that $c_p^{v,A} = c_e^v + c_s^v$. As the particle volume fractions, $c_p^{v,B}$, can theoretically be in the range [0,1], these differences between the two data points at each composition are small. The number of particles per volume is plotted for each of the five packs in Figure 13, where N_p is the number of particles in the VOI. The number of total particles increases with increasing weight % of

16

Pack [% wt.]	0	25	50	75	100
W_e [g]	100.001	74.998	50.003	25.007	0.000
W_s [g]	0.000	24.997	50.003	75.002	100.000
D [mm]			—— 57.67 ——		-
D_{VOI} [mm]			—— 46.57 ——		-
Higher Volume Fraction Packs					
H [mm]	41.43	42.74	48.51	50.04	51.42
H_{VOI} [mm]	30.33	31.64	37.41	38.93	40.32
ε_{IP} [%]	2.23	2.85	2.60	2.72	3.66
Lower Volume Fraction Packs					
H [mm]	41.22	43.10	46.22	49.62	49.76
H_{VOI} [mm]	30.12	31.99	35.12	38.52	38.66
ε_{IP} [%]	2.22	2.72	2.46	2.66	3.52

TABLE I. Description of randomized packs. W_s and W_e are the weights of each particulate phase (s subscript for sphere and e subscript for ellipsoid).
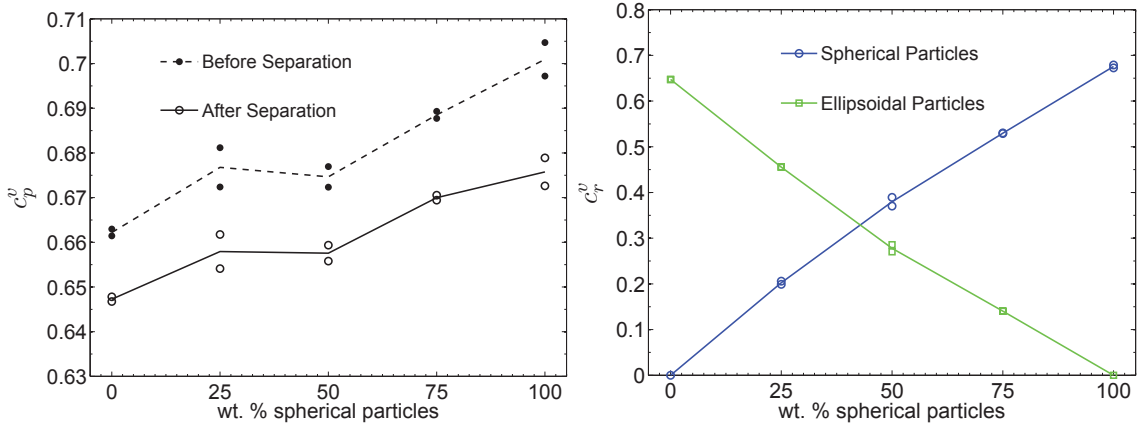
FIG. 12. Volume fraction plots for various compositions of the surrogate system. Note that two samples for each composition were studied and are referred to as higher volume fraction packs (top points) and lower volume fraction packs (bottom points).

spherical particles, because the volume of a spherical particle is smaller than the volume of an ellipsoidal particle as evident in the distribution of particles for the 50% pack in Figure
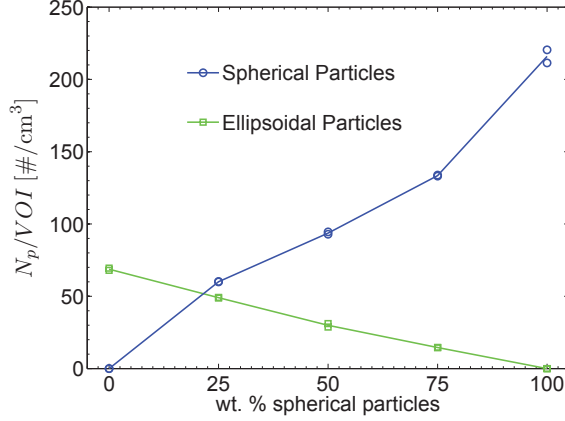
FIG. 13. Number of particles per cm^3.

7(b). The mean and max errors between the voxel particles and their corresponding ideal ellipsoidal representation are presented in Table II. All mean errors for each pack are below 5%. As discussed earlier, the noticeable maximum errors in the surface area are related to errors in representing the surface of voxel particles. Moreover, the noticeable maximum errors for Π_2 exist for a small number of particles that do not match an ellipsoid well. Overall, the low errors achieved throughout the microstructure characterization process show that the sample preparation, data acquisition, and image processing steps produce scientifically sound and repeatable results with well controlled errors.

The mixture of randomized ellipsoids (0% wt. spherical particles) has a volume fraction consistent with packing simulations of monodisperse ellipsoids reaching a maximally random jammed state [51]. For the average size ellipsoidal particle in this work ($a = 3.04$ mm, $b = 1.11$ mm, and $c = 0.83$ mm), a maximum packing volume fraction can be extrapolated to be 0.68 from the work of Chaikin et al. [51] ($c_p^{v,B} = 0.66$ in this work). It is expected that this volume fraction should be similar as the ellipsoidal particles have a small range in size as seen in Figure 7. The volume fraction of maximally jammed monodisperse spheres in the work of Chaikin et al. [51] is 0.64, and the volume fractions for the compositions with 100% spheres considered in this work is higher ($c_p^{v,B} = 0.70$ from Figure 12) due to the polydispersity as evidenced by the range in sizes in Figure 7. Note that this volume fraction falls below 0.74, the assumed maximum achievable volume fraction of monodisperse spheres first proposed by Keplar and supported by many thereafter [8]. When considering all of the randomized compositions, there is a monotonically increasing trend in volume fraction, c_p^v.

18

Pack [% wt.]	0	25	50	75	100
	Higher Volume Fraction Packs				
ΔV (mean)	0.65	0.50	0.41	0.33	0.41
ΔV (max)	3.63	3.29	3.29	3.27	3.69
ΔS (mean)	4.11	3.16	2.56	2.03	2.62
ΔS (max)	34.22	28.55	28.62	28.15	35.28
$\Delta \Pi_2$ (mean)	1.09	0.56	0.38	0.22	0.21
$\Delta \Pi_2$ (max)	14.17	8.41	8.37	5.68	18.69
	Lower Volume Fraction Packs				
ΔV (mean)	0.63	0.52	0.35	0.32	0.40
ΔV (max)	3.69	3.52	3.50	3.22	3.54
ΔS (mean)	3.99	3.31	2.17	2.04	2.50
ΔS (max)	35.81	32.26	26.05	27.56	32.71
$\Delta \Pi_2$ (mean)	1.05	0.57	0.36	0.22	0.21
$\Delta \Pi_2$ (max)	6.47	12.79	11.43	4.97	10.09

TABLE II. Summary of errors between voxel particles and idealized ellipsoids. The unit of all values is %. Less than 0.1% of all particles considered in these mixtures have $\Delta \Pi_2 > 5\%$, and less than 14.3% of all particles have $\Delta S > 5\%$

It is known that when the scales of two inclusions are significantly different, the mixtures will have higher volume fractions than the maximum volume fractions of a single constituent for monomodal spheres [52]. However, as the smallest semiaxes of the ellipsoids are similar to the average radius of the spherical particles, no such effect is observed.

The distributions of particle orientations for the randomized pack with 100% weight of ellipsoids is shown in Figure 14. Notice that there is no preference of the randomized pack's ellipsoids azimuthal angle, θ_a (compare with Figure 11 for semi-ordered pack). Moreover, there is a low probability that particles are suspended in the unstable vertical position, $\phi_a = 0°$. This randomness in the azimuthal angle, θ_a, confirms the randomizing effects in the sample preparation steps. The ellipsoidal particles in the other randomized packs exhibit similar trends in their orientations and are not reported here.
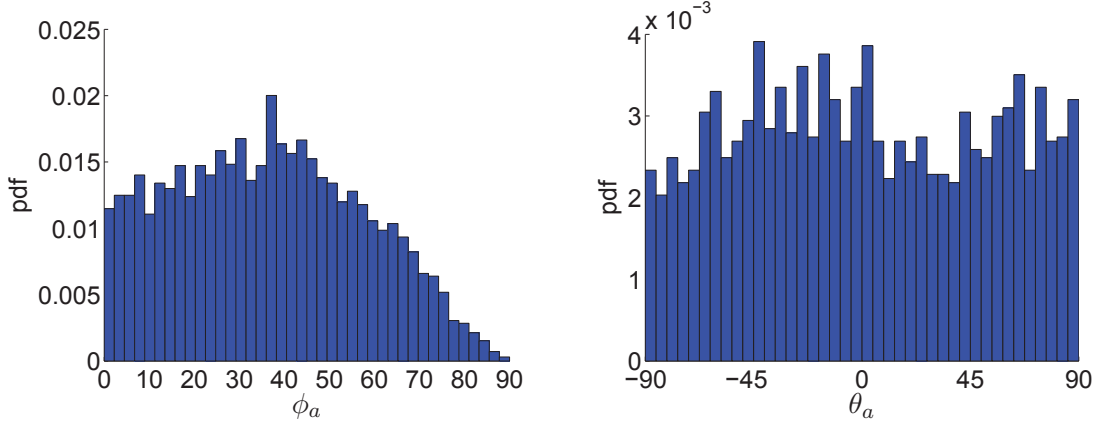
FIG. 14. Distribution of orientations for ellipsoidal particles in the pack with 0% weight of spherical particles.

When comparing the semi-ordered pack of ellipsoids to the randomized one, the volume fraction of the semi-ordered ellipsoid pack is higher. This is in agreement with studies of ordered packs of monodisperse ellipsoids, as they are known to have a maximum particle volume fraction of $0.74 - 0.77$ [53]. When comparing the altitude angle, ϕ_a, distributions between the semi-ordered and randomized pack, there is a higher probability of the semi-ordered pack particles existing in the xy plane ($\phi_a = 0°$) and a preferred direction for θ_a (see Figures 11 and 14).

Let us note that the microstructure characterization method presented in this work can be used in a variety of applications as well as in validation of packing simulations [10, 54]. In this work, the datasets provide a foundational set for considering the microstructure's effect on overall properties, and the effect of these packing configurations on the overall anisotropic thermal conductivity tensor will be explored in the remainder of this paper.

III. THEORETICAL OVERVIEW OF OVERALL ANISOTROPIC PROPERTIES

Using the Hashin-Shtrikman variational principle and assuming that particulate composites are homogeneous and ergodic, Willis formulated a second-order approximation of bounds on elastic and conductivity constants in which the two-point probability functions are embedded within the mathematical formulation directly [28]. In Willis' work, assumptions about the configuration of the particles were made when computing overall properties. In this work, upper and lower anisotropic bounds as well as anisotropic self-consistent esti-

mates are computed for the first time to the best of our knowledge without assumptions of statistical isotropy nor ellipsoidal or any other material symmetry for complex tomographically characterized polydisperse microstructures. A simple overview of theory is discussed next.

A.   n-point Probability Functions

As described in [16, 42], the n-point probability functions are derived using a phase indicator function at a position $\boldsymbol{x}$ in a sample α of an ensemble space $\mathcal{E}$:

$$\chi_r(\boldsymbol{x}; \alpha) = \begin{cases} 1 & \text{if } \boldsymbol{x} \text{ in phase } r \\ 0 & \text{otherwise.} \end{cases} \tag{7}$$

An ensemble is a collection of material samples being considered. The ensemble average is given by

$$\overline{\chi_r(\boldsymbol{x})} = \int_{\mathcal{E}} \chi_r(\boldsymbol{x}; \alpha) p(\alpha) \mathrm{d}\alpha, \tag{8}$$

where $p(\alpha)$ is the probability density function of α in $\mathcal{E}$. The n-point probability function, $S_{r_1 r_2 \cdots r_n}(\boldsymbol{x}_1, \boldsymbol{x}_2, \cdots, \boldsymbol{x}_n)$, is defined as

$$S_{rs\cdots q}(\boldsymbol{x}_1, \boldsymbol{x}_2, \cdots, \boldsymbol{x}_n) = \overline{\chi_r(\boldsymbol{x}_1)\chi_s(\boldsymbol{x}_2) \cdots \chi_q(\boldsymbol{x}_n)}. \tag{9}$$

It represents the probability of phases $r, s, \cdots, q$ existing at points $\boldsymbol{x}_1, \boldsymbol{x}_2, \cdots, \boldsymbol{x}_n$, simultaneously. In general, the probability functions for a heterogeneous material are spatially complex. In this work, a second-order model for computing bounds on overall anisotropic thermal conductivity is considered.

For statistical homogeneous materials, where the probability functions are translationally invariant, the one-point probability function attains a constant value, $S_r(\boldsymbol{x}) = c$, and the two-point function simplifies to $S_{rs}(\boldsymbol{x}, \boldsymbol{x}') = S_{rs}(\boldsymbol{x} - \boldsymbol{x}')$. For statistically homogeneous systems, it is meaningful to define volume averages. When assuming ergodicity of homogeneous systems, ensemble averaging is equivalent to volume averaging in the infinite volume limit

$$S_{rs\cdots q}(\boldsymbol{x}_1, \boldsymbol{x}_2, \cdots, \boldsymbol{x}_n) = \\ \lim_{\Omega \to \infty} \frac{1}{\Omega} \int_{\Omega} \chi_r(\boldsymbol{x}_1 - \boldsymbol{l})\chi_s(\boldsymbol{x}_2 - \boldsymbol{l}) \cdots \chi_q(\boldsymbol{x}_n - \boldsymbol{l}) \, \mathrm{d}\Omega, \tag{10}$$

21

where $\boldsymbol{l}$ is a translation vector, and Ω is the volume of the domain. For homogeneous and ergodic systems, the one-point probability function is equivalent to the volume fraction of phase r ($S_r(\boldsymbol{x}) = c_r$). The two-point probability functions of a statistically homogeneous and isotropic system (rotationally and translationally invariant) are defined as $S_{rs}(\boldsymbol{x}, \boldsymbol{x}') = S_{rs}(|\boldsymbol{x} - \boldsymbol{x}'|)$, where the function only depends on the distance between two points. For homogeneous systems with no long-range order, we observe two limit cases in the pointwise sense of the two-point probability functions, which can be expressed as

$$S_{rs}(\boldsymbol{x} - \boldsymbol{x}') \rightarrow \begin{cases} c_r \delta_{rs} & \text{as } \boldsymbol{x} - \boldsymbol{x}' \rightarrow \boldsymbol{0} \\ c_r c_s & \text{as } \boldsymbol{x} - \boldsymbol{x}' \rightarrow \infty, \end{cases} \tag{11}$$

where δ_{rs} is the Kronecker delta. More information on the n-point probability functions can be found in work by Torquato [55] and Beran [56]. In this work, statistically anisotropic systems are considered, and n-point probability functions are used when addressing the issues of material order.

B.   Hashin-Shtrikman Variational Principle

The Hashin-Shtrikman variational principle is employed to obtain bounds on thermal-mechanical properties of an anisotropic material as described in [27, 28]. This paper focuses on computing the overall bounds and self-consistent estimates for the anisotropic thermal conductivity tensor. Note that this formulation is similar to theory for overall linear elastic constants [42].

It is assumed that the material follows a constitutive relation of $\boldsymbol{q} = \partial w(\boldsymbol{Q})/\partial \boldsymbol{Q}$, where $w(\boldsymbol{Q})$ is an energy density function, $\boldsymbol{q}$ is the heat flux vector, and $\boldsymbol{Q} = -\nabla T$ is the negative temperature gradient for a temperature T at a point $\boldsymbol{x}$. When the material obeys Fourier's law, $\boldsymbol{q} = \boldsymbol{\kappa} \cdot \boldsymbol{Q}$ (linear constitutive relation), the energy density function is defined as $w(\boldsymbol{Q}) = (\boldsymbol{Q} \cdot \boldsymbol{\kappa} \cdot \boldsymbol{Q})/2 \geq 0$, where $\boldsymbol{\kappa}$ is the symmetric positive semi-definite second order thermal conductivity tensor. This symmetric positive semi-definiteness requirement is in agreement with Onsager's reciprocity theorem [57]. Thus, the generally anisotropic conductivity tensor computed in this work has six independent components. A complementary energy density, $w^*(\boldsymbol{q})$, can also be defined, where $w^*(\boldsymbol{q}) + w(\boldsymbol{Q}) = \boldsymbol{q} \cdot \boldsymbol{Q}$ and $\boldsymbol{Q} = \partial w^*(\boldsymbol{q})/\partial \boldsymbol{q}$. For a material following Fourier's law, $w^* = (\boldsymbol{q} \cdot \boldsymbol{\rho} \cdot \boldsymbol{q})/2 \geq 0$, where $\boldsymbol{\rho}$ represents the symmetric positive

semi-definite second order thermal resistivity tensor. Note that $\boldsymbol{\rho} = \boldsymbol{\kappa}^{-1}$. The internal energy and complementary internal energy of the system are defined as $E = \int_\Omega w \, d\Omega$ and $E^* = \int_\Omega w^* \, d\Omega$, respectively.

$$T = \hat{T} \;\text{on}\; \partial\Omega \qquad T_0 = \hat{T} \;\text{on}\; \partial\Omega \qquad T' = 0 \;\text{on}\; \partial\Omega$$

LB $\boldsymbol{\kappa}$ = $\boldsymbol{\kappa}_0$ + $\boldsymbol{\kappa}_0, \boldsymbol{p}$

UB $\boldsymbol{\rho}$ = $\boldsymbol{\rho}_0$ + $\boldsymbol{\rho}_0, \boldsymbol{t}$

$$q_n = \hat{q}_n \;\text{on}\; \partial\Omega \qquad q_n^0 = \hat{q}_n \;\text{on}\; \partial\Omega \qquad q_n' = 0 \;\text{on}\; \partial\Omega$$

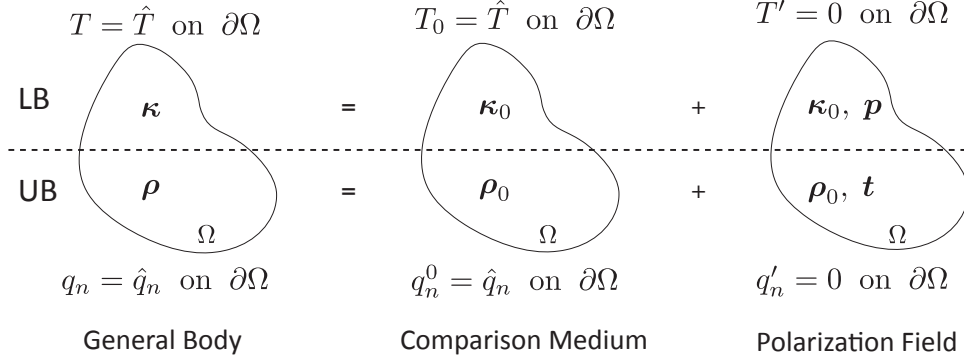General Body   Comparison Medium   Polarization Field

FIG. 15. Body decomposition with prescribed Dirischlet and Neumann boundary conditions, respectively, corresponding to the lower bound and upper bound formulations.

Hashin and Shtrikman [27] proposed the body decomposition, as shown in Figure 15. The top half of this figure shows the body decomposition with a prescribed temperature field on the boundary, $\hat{T}$, which is used to compute the lower bound (LB) of the overall $\overline{\boldsymbol{\kappa}}$. The bottom half of this figure shows the decomposition for a body with a prescribed normal heat flux, $\hat{q}_n$, and this formulation is used for computing the lower bound of the overall $\overline{\boldsymbol{\rho}}$, corresponding to the upper bound (UB) of $\overline{\boldsymbol{\kappa}}$. Note that quantities with $\bar{\bullet}$ denote an overall or volume averaged quantity, $\bar{\bullet} = 1/\Omega \int \bullet \, d\Omega$. The governing equations of the corresponding elliptic boundary value problems are given by

LB: UB:

$$\nabla \cdot \left[\boldsymbol{\kappa}_0 \cdot \boldsymbol{Q} + \boldsymbol{p} \right] = 0 \quad \text{in} \quad \Omega, \qquad\qquad \nabla \cdot \boldsymbol{q} = 0 \quad \text{in} \quad \Omega,$$
$$\boldsymbol{p} - \left[\boldsymbol{\kappa} - \boldsymbol{\kappa}_0 \right] \cdot \boldsymbol{Q} = 0 \quad \text{in} \quad \Omega, \qquad\qquad \boldsymbol{t} - \left[\boldsymbol{\rho} - \boldsymbol{\rho}_0 \right] \cdot \boldsymbol{q} = 0 \quad \text{in} \quad \Omega,$$
$$T' = 0 \quad \text{on} \quad \partial\Omega, \qquad\qquad\qquad\qquad \boldsymbol{q}' \cdot \boldsymbol{n} = 0 \quad \text{on} \quad \partial\Omega,$$

(12)   (13)

where $\boldsymbol{\kappa}_0$ is the thermal conductivity tensor of a comparison medium, and $\boldsymbol{p}$ is the heat flux polarization tensor. T_0 and T' represent the homogeneous and fluctuation temperature fields, respectively. $\boldsymbol{q}'$ is the heat flux fluctuation field, $\boldsymbol{\rho}_0$ is the comparison medium resistivity tensor, $\boldsymbol{t}$ is the temperature gradient polarization field, $q_n = \boldsymbol{q} \cdot \boldsymbol{n}$ is the normal heat flux, and $\boldsymbol{n}$ is the unit normal vector. Formulations equivalent to the ones described by the

23

strong forms (12) and (13) can be obtained by minimizing the functionals

LB:

$$2\mathcal{F}(\boldsymbol{p}) = \int_\Omega \left[\boldsymbol{p} \cdot [\boldsymbol{\kappa} - \boldsymbol{\kappa}_0]^{-1} \cdot \boldsymbol{p} + \boldsymbol{p} \cdot \int_{\Omega_{x'}} \boldsymbol{\Gamma}(\boldsymbol{x}, \boldsymbol{x}') \cdot [\boldsymbol{p}(\boldsymbol{x}') - \bar{\boldsymbol{p}}] \mathrm{d}\Omega_{x'} - 2\boldsymbol{p} \cdot \boldsymbol{Q}_0 \right] \mathrm{d}\Omega, \tag{14}$$

and

UB:

$$2\mathcal{F}^*(\boldsymbol{t}) = \int_\Omega \left[\boldsymbol{t} \cdot [\boldsymbol{\rho} - \boldsymbol{\rho}_0]^{-1} \cdot \boldsymbol{t} + \boldsymbol{t} \cdot \int_{\Omega_{x'}} \boldsymbol{U}(\boldsymbol{x}, \boldsymbol{x}') \cdot [\boldsymbol{t}(\boldsymbol{x}') - \bar{\boldsymbol{t}}] \mathrm{d}\Omega_{x'} - 2\boldsymbol{t} \cdot \boldsymbol{q}_0 \right] \mathrm{d}\Omega, \tag{15}$$

for the lower and upper bound formulations, respectively. $\boldsymbol{\Gamma}(\boldsymbol{x}, \boldsymbol{x}')$ is the second order linear operator related to the Green's function solution. $\boldsymbol{Q}_0$ denotes the negative temperature gradient in a homogeneous comparison medium, and $\boldsymbol{q}_0$ is the homogeneous heat flux. Note that the energy functional is defined as $\mathcal{F} = E_0 - E$, where E_0 is the internal energy of the comparison medium. $\mathcal{F}^* = E_o^* - E^*$, where E_0^* is the complementary internal energy of the comparison medium. For the upper bound formulation, $\boldsymbol{U}$ is the second order linear operator related to the Green's function solution ($\boldsymbol{U} = \boldsymbol{\kappa} - \boldsymbol{\kappa} \cdot \boldsymbol{\Gamma} \cdot \boldsymbol{\kappa}$).

To find second-order estimates to the stationary point of Equations (14) and (15), trial fields of $\boldsymbol{p}$ and $\boldsymbol{t}$ are assumed piecewise-constant in each phase r ($\boldsymbol{p}^* = \sum_{r=0}^n \chi_r \boldsymbol{p}_r$ and $\boldsymbol{t}^* = \sum_{r=0}^n \chi_r \boldsymbol{t}_r$ for a system of n particulate phases and a matrix corresponding to $r = 0$). The following systems of equations are obtained after discretization of the polarizations fields, $\boldsymbol{p}$ and $\boldsymbol{t}$, averaging over the ensemble space $\mathcal{E}$ and using the calculus of variations

LB:

$$c_r(\boldsymbol{\kappa}_r - \boldsymbol{\kappa}_0)^{-1} \cdot \boldsymbol{q}_r + \sum_{s=0}^n \int_{\Omega_{\boldsymbol{x}'}} \boldsymbol{\Gamma}^\infty(\boldsymbol{x} - \boldsymbol{x}')(S_{rs}(\boldsymbol{x} - \boldsymbol{x}') - c_r c_s) \cdot \boldsymbol{q}_s \, \mathrm{d}\Omega_{\boldsymbol{x}'} = -c_r \overline{\boldsymbol{Q}}, \tag{16}$$

and

UB:

$$c_r(\boldsymbol{\rho}_r - \boldsymbol{\rho}_0)^{-1} \cdot \boldsymbol{t}_r + \sum_{s=0}^n \int_{\Omega_{\boldsymbol{x}'}} \boldsymbol{U}^\infty(\boldsymbol{x} - \boldsymbol{x}')(S_{rs}(\boldsymbol{x} - \boldsymbol{x}') - c_r c_s) \cdot \boldsymbol{t}_s \, \mathrm{d}\Omega_{\boldsymbol{x}'} = -c_r \overline{\boldsymbol{q}}. \tag{17}$$

Here c_r and c_s are the volume fractions of phase r and s, respectively, $\boldsymbol{\kappa}_r$ is the thermal conductivity tensor of phase r, while $\overline{\boldsymbol{Q}}$ is the overall negative temperature gradient. $\boldsymbol{\Gamma}^\infty$ and $\boldsymbol{U}^\infty$ are related to the Green's function solution for an infinite body. For the upper bound formulation, $\boldsymbol{\rho}_r$ is the resistivity tensor of phase r, while $\bar{\boldsymbol{q}}$ is the overall heat flux.

24

These systems of equations are solved for the piecewise-constant fields, $\boldsymbol{p}_r$ and $\boldsymbol{t}_r$, to find the mean polarization fields, $\overline{\boldsymbol{p}} = \sum_{r=0}^{n} c_r \boldsymbol{p}_r$ and $\overline{\boldsymbol{t}} = \sum_{r=0}^{n} c_r \boldsymbol{t}_r$. The volume averaged constitutive relations,

$$\text{LB:} \qquad\qquad \text{UB:}$$
$$\overline{\boldsymbol{q}} = \overline{\boldsymbol{\kappa}} \cdot \overline{\boldsymbol{Q}} = \boldsymbol{\kappa}_0 \cdot \overline{\boldsymbol{Q}} + \overline{\boldsymbol{p}}, \qquad \overline{\boldsymbol{Q}} = \overline{\boldsymbol{\rho}} \cdot \overline{\boldsymbol{q}} = \boldsymbol{\rho}_0 \cdot \overline{\boldsymbol{q}} + \overline{\boldsymbol{t}}, \tag{18}$$

are used to calculate the overall $\overline{\boldsymbol{\kappa}}$ and $\overline{\boldsymbol{\rho}}$, respectively. When $\boldsymbol{\kappa}_r - \boldsymbol{\kappa}_0$ is the smallest positive semi-definite matrix for all phases r in the lower bound formulation, the resulting $\overline{\boldsymbol{\kappa}}$ is the second-order lower bound of the conductivity tensor. Meanwhile, when $\boldsymbol{\rho}_r - \boldsymbol{\rho}_0$ is the smallest positive semi-definite matrix for all phases r in the upper bound formulation, the second-order lower bound of the resistivity tensor is obtained (upper bound of the conductivity tensor, $\overline{\boldsymbol{\kappa}} = \overline{\boldsymbol{\rho}}^{-1}$).

Another widely used model for computing overall material properties is the self-consistent estimate (SC). As described in Willis' work [28], self-consistent estimates are calculated by minimizing the volume averaged energy and complementary energy functionals $|\overline{\mathcal{F}}| = |E_0 - \overline{E}|$ and $|\overline{\mathcal{F}}^*| = |E_0^* - \overline{E}^*|$. This leads to $\overline{E} = E_0$ ($\overline{\boldsymbol{\kappa}} = \boldsymbol{\kappa}_0$) and $\overline{E}^* = E_0^*$ ($\overline{\boldsymbol{\rho}} = \boldsymbol{\rho}_0$). With this in mind, the following objective functions are minimized in order to compute self-consistent estimates

$$\text{SC-L:} \qquad\qquad \text{SC-U:}$$
$$\Pi_{SC}^L = ||\boldsymbol{\kappa}_0 - \overline{\boldsymbol{\kappa}}||_{\mathbb{F}} \qquad \Pi_{SC}^U = ||\boldsymbol{\rho}_0 - \overline{\boldsymbol{\rho}}||_{\mathbb{F}}. \tag{19}$$

The integrals presented in Eq. (16) and (17) and consequently in (19), which are products of the tensors related to the Green's function solution, $\boldsymbol{\Gamma}^\infty$ and $\boldsymbol{U}^\infty$, and the second-order probability function, are strenuous especially near the origin due to the singularity of $\boldsymbol{\Gamma}^\infty$ and $\boldsymbol{U}^\infty$. Note that for statistically isotropic systems and systems with aligned ellipsoids, these integrals can be calculated analytically leading to a closed form solution of the overall conductivity tensor. Closed form solutions using these assumptions have been presented in work by Willis [28] and Weng [58], just to name a few. This work is not limited by these assumptions, and the integral kernels are calculated numerically using the adaptive sparse-grid Smolyak integration method with hierarchical basis that was developed in our previous work [42].

IV. STATISTICAL CHARACTERIZATION

After the voxel data is processed, the packs are statistically characterized by computing one- and two-point probability functions directly from the voxel data using our parallel statistical sampling code, STAT3D [16]. Note that sampling in $\mathbb{R}^3$ on idealized packs as done in [16] is also possible and would result in nearly identical results as shown in [22]. We do not present this verification here. This section presents the statistical functions for compositions described in section II E. The semi-ordered pack and one realization of each randomized composition (higher volume fraction packs as shown in Figure 12(a)) are statistically characterized.

As presented in [16], a spherical sampling template is used to compute n-point probability functions. After a convergence study, the sampling template was discretized with 2000 radial points and 32 circumferential points and was randomly thrown into the sample 10 million times. Note that this very high sampling frequency is important for resolving the probability functions. In order to quantify the errors in the statistical functions, we consider the limit cases of the two-point probability functions as given by Eq. (11). The following error measures at the origin and at a far distance are used

$$0 \leq \varepsilon_{S_{rs}(\mathbf{0})} = \frac{\left| S_{rs}\left(\mathbf{0}\right) - c_r^v \delta_{rs} \right|}{c_r^v} \times 100 \ [\%], \tag{20}$$

$$0 \leq \varepsilon_{S_{rs}(\boldsymbol{\infty})} = \frac{\mathrm{std}\left(S_{rs}\left(\boldsymbol{\infty}\right) - c_r^v c_s^v \right)}{c_r^v c_s^v} \times 100 \ [\%], \tag{21}$$

where std($\bullet$) is the standard deviation.

If a pack is perfectly isotropic, the standard deviations in the two-point probability functions at $|\boldsymbol{x} - \boldsymbol{x}'|$ are zero (std($S_{rs}(\boldsymbol{x} - \boldsymbol{x}')|_{|\boldsymbol{x}-\boldsymbol{x}'|}) = 0$). For random statistically homogeneous mixtures, short range statistical anisotropy can exist due to both the shape of the particles and/or the configuration of the particles, and no long range order is expected for randomized systems. A specific case of statistically anisotropic systems, considered in previous works [27, 28], is when the two-point probability functions exhibit ellipsoidal symmetry, which is known to occur for ordered packs of randomly positioned and uniformly aligned monodisperse ellipsoids. Ellipsoidal symmetry means that the function values of $S_{rs}(\boldsymbol{x} - \boldsymbol{x}')$ are constant on contours of an ellipsoid,

$$(\boldsymbol{x} - \boldsymbol{x}')^T \boldsymbol{B}^{-1} (\boldsymbol{x} - \boldsymbol{x}'), \tag{22}$$

26

where $\boldsymbol{B}$ is a positive definite matrix whose eigenvalues are the squares of an ellipsoid's semiaxes. It will be shown that the statistical descriptors of the polydisperse packs considered in this work do not exhibit ellipsoidal symmetry. When ellipsoidal symmetry does not exist, closed-form solutions of the overall properties as presented in [28] and many papers thereafter can not be obtained.
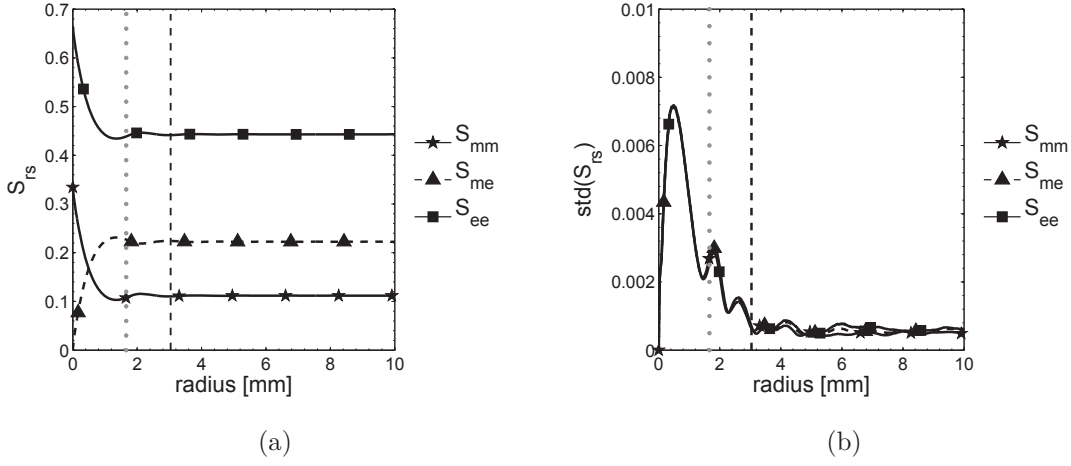
A. Semi-ordered Pack

FIG. 16. Mean and standard deviation of two-point probability functions for semi-ordered pack of ellipsoids from Figure 9.

In what follows, the subscripts m, s and e are used to refer to the matrix, spherical particles (mustard seeds), and ellipsoidal particles (rice grains), respectively. The one-point probability functions for the semi-ordered mixture of ellipsoids (see Figure 9) are $c_m = 0.3345$ and $c_e = 0.6655$. The mean and standard deviations of the two-point probability functions are presented in Figure 16. The maximum errors, as defined by Equations (20) and (21) for all two-point probability functions of this mixture are $\varepsilon_{S_{rs}(\boldsymbol{0})} = 0.0059\%$ and $\varepsilon_{S_{rs}(\boldsymbol{\infty})} = 0.304\%$, respectively. As can be seen in Figure 16(a), the mean two-point probability values reach local extrema near the average semiaxis, $(a+b+c)/3 = 1.66$ mm (vertical gray dotted line) and the largest semiaxis (vertical black dashed line). Note that the average semiaxes of ellipsoids in this work are $a = 3.04$ mm, $b = 1.111$ mm, and $c = 0.83$ mm. Considering the mean function values and the standard deviations as $(\boldsymbol{x}-\boldsymbol{x'}) \rightarrow \infty$ (Figure 16), the functions are considered converged when $|\boldsymbol{x}-\boldsymbol{x'}| = 8$ mm, resulting in a characteristic material length

scale of 16 mm (twice the radius). The characteristic material length scale can be considered as the optimal size of a Representative Unit Cell (RUC) [16]. This length scale is $\sim 20\times$ the smallest semi-axis and $\sim 5\times$ the largest semi-axis. The characteristic material length scale is important in this work, as the saturation of the probability functions guarantee the convergence of the integrals in Equations (16), (17) and (19) as $(\boldsymbol{x} - \boldsymbol{x}') \rightarrow \infty$ [28]. Also of interest in Figure 16(b) is where the maximum standard deviations occur, since the $\text{std}(S_{rs})$ represents how anisotropic the system is. The largest peak occurs near a distance from the origin of the smallest semiaxis ($c = 0.83$ mm), the second peak near the average semiaxis (dotted gray line), and the deviations diminish after the distance near the largest semiaxis (dashed black line). Note that these deviations are related to a combination of the particle shape, the polydispersity, and the configuration. While these deviations are less than 6% of the function values, this statistical anisotropy will lead to larger macroscopic anisotropy of the thermal conductivity tensor, because the anisotropy in morphology is amplified by the local anisotropic material constants.

One of the two-point probability functions, S_{ee}, is visualized in Figure 17. Notice again that local minima exist near distances from the origin to the average semiaxis and the largest semiaxis lengths. The anisotropic nature of the two-point probability function in the xy and yz plane (Figure 17(c) and 17(d), respectively) is due to the preferred alignment of the particles in the y direction (see Figure 11). While the general shape of this statistical function is ellipsoidal, notice that S_{22} does not exhibit complete ellipsoidal symmetry (given by Equation (22)), thus prohibiting the closed form integration given in [28]. Near spherical symmetry occurs only in the xz plane (Figure 17(b)) since the smallest semiaxes of the averaged size ellipsoid are similar ($b = 1.11$ mm, and $c = 0.83$ mm). Note that for a semi-ordered pack (based on our packing method meaning not randomly positioned and uniformly aligned inclusions) of ellipsoids in which all semi-axes are significantly different, ellipsoidal symmetry would not be present in any plane.

B. Randomized Packs

The mean and standard deviations of the two-point probability functions for selected randomized compositions are considered in Figures 18(a)-(f). The maximum errors, as defined by Equations (20) and (21), for all two-point probability functions of the five randomized
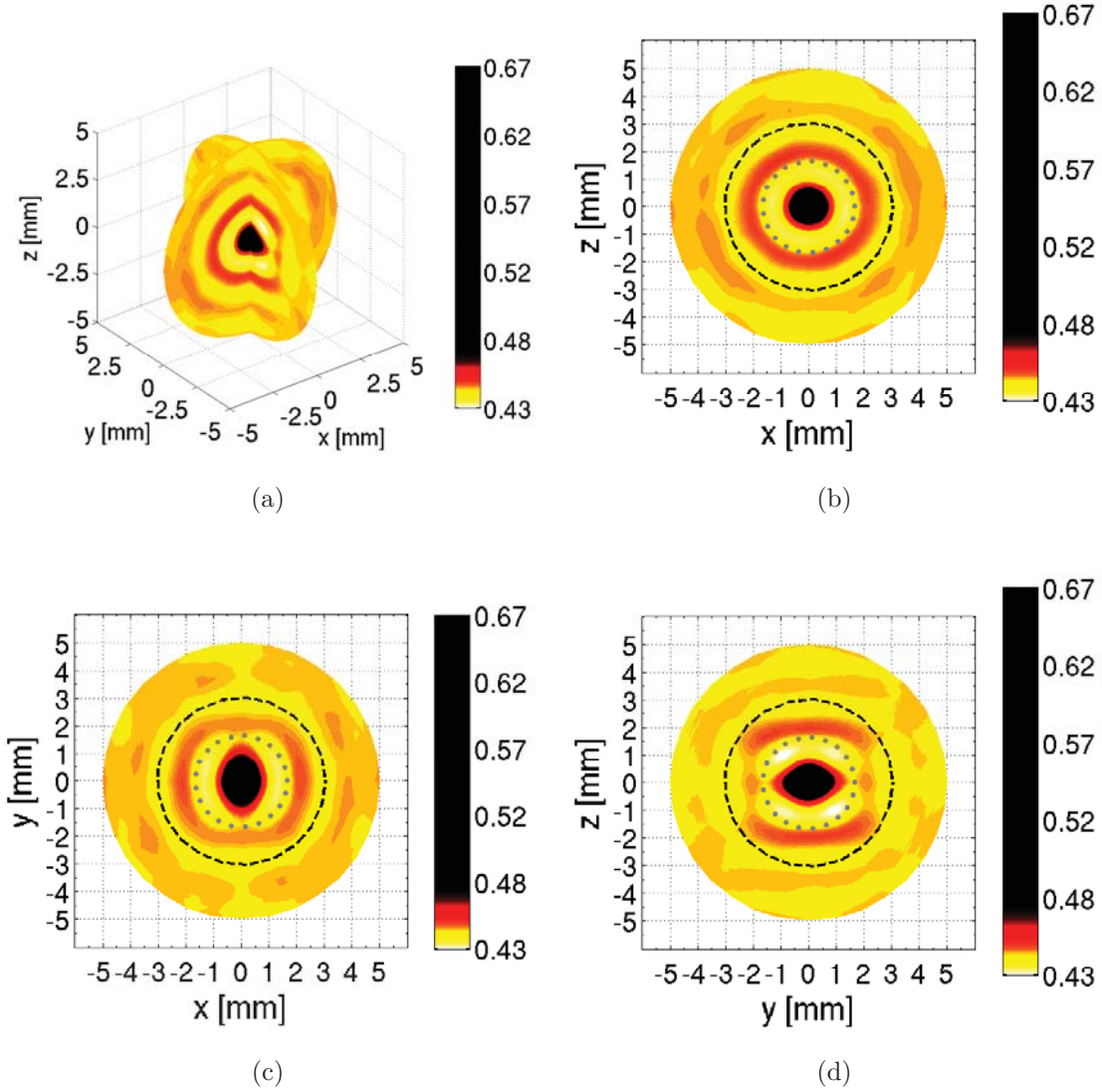
28

FIG. 17. (a) 3D representation of $S_{ee}(\boldsymbol{x} - \boldsymbol{x}')$. (b)-(d) show that $S_{ee}(\boldsymbol{x} - \boldsymbol{x}')$ in the xz, xy and yz planes, respectively. Note that the scale of the colorbar is adjusted to highlight where local minima of this function exist.

compositions are $\varepsilon_{S_{rs}(\boldsymbol{0})} = 0.104\%$ and $\varepsilon_{S_{rs}(\boldsymbol{\infty})} = 4.146\%$, respectively. Note that the spike in the standard deviations at the origin in Figure 18(f) (less than 1% of the function value) occurs at the voxel resolution of the dataset, $|\boldsymbol{x} - \boldsymbol{x}'| \approx 0.07$ mm. This is a numerical artifact due to the discontinuities associated with the voxelization of data. In Figure 18(d), the standard deviations for the 50% pack as $(\boldsymbol{x} - \boldsymbol{x}') \to \infty$ are not fully saturating for some of functions. This indicates that larger samples might be needed for better resolution. Nevertheless, these functions are not significantly misrepresenting the statistical anisotropy

in the system, since the standard deviations as $(\boldsymbol{x} - \boldsymbol{x}') \rightarrow \infty$ are on the same order as the standard deviation peaks near the origin. For the 25% and 75% compositions, the standard deviations as $(\boldsymbol{x} - \boldsymbol{x}') \rightarrow \infty$ are similar to those for the 50% mixture. The general trend shows that the maximum standard deviations for the two-point probability functions of the mixtures decrease as the amount of spheres in the system increases (Figures 18(b), (e), and (f)), indicating that the spherical particles tend to organize randomly (isotropically). For the 100% mixture of spheres, the deviations are essentially zero (Figure 18(f)), indicating the pack is nearly isotropic. This trend in statistical anisotropy will be reflected in the macroscopic anisotropy of the thermal conductivity tensor. Once more, individual local minima and corresponding high standard deviations are due to particle shape and the spatial organization.

Considering both the deviations as $(\boldsymbol{x} - \boldsymbol{x}') \rightarrow \infty$ and where the two-point probability functions saturate, characteristic material length scales are determined for the mixtures. The mixtures with only one particulate phase (0% and 100% weight of spherical particles) have a characteristic material length scale around 16 mm, as the functions converge at $|\boldsymbol{x} - \boldsymbol{x}'| = 8$ mm. This same length scale is attributed to the similarity in the average semiaxis length of the ellipsoids, $(a + b + c)/3 = 1.66$ mm, and the radius of the average sphere, 0.94 mm. The three phase mixtures (25%, 50% and 75% weight of spherical particle packs) have larger characteristic material length scales, 20 mm. This larger length scale is expected because more interactions must be captured as polydispersity grows.

When comparing the probability functions of the randomized pack of 100% ellipsoids to the semi-ordered pack of ellipsoids, the amount of statistical anisotropy reflects the differences in configuration. The maximum standard deviation for the randomized pack of ellipsoids is $\mathrm{std}(S_{rs}) = 0.0049$ (see Figure 18(b)), which is smaller than the maximum standard deviation of the semi-ordered pack $\mathrm{std}(S_{rs}) = 0.0072$ (Figure 16(b)), and indicates less statistical anisotropy. Also note that there are only two maxima in the standard deviations as compared to three for the semi-ordered pack (compare Figures 16(b) and 18(b)). As there is no apparent alignment in the xy plane for the randomized pack (Figure 14), the two-point probability functions reflect this behavior and smooth out these standard deviation peaks.
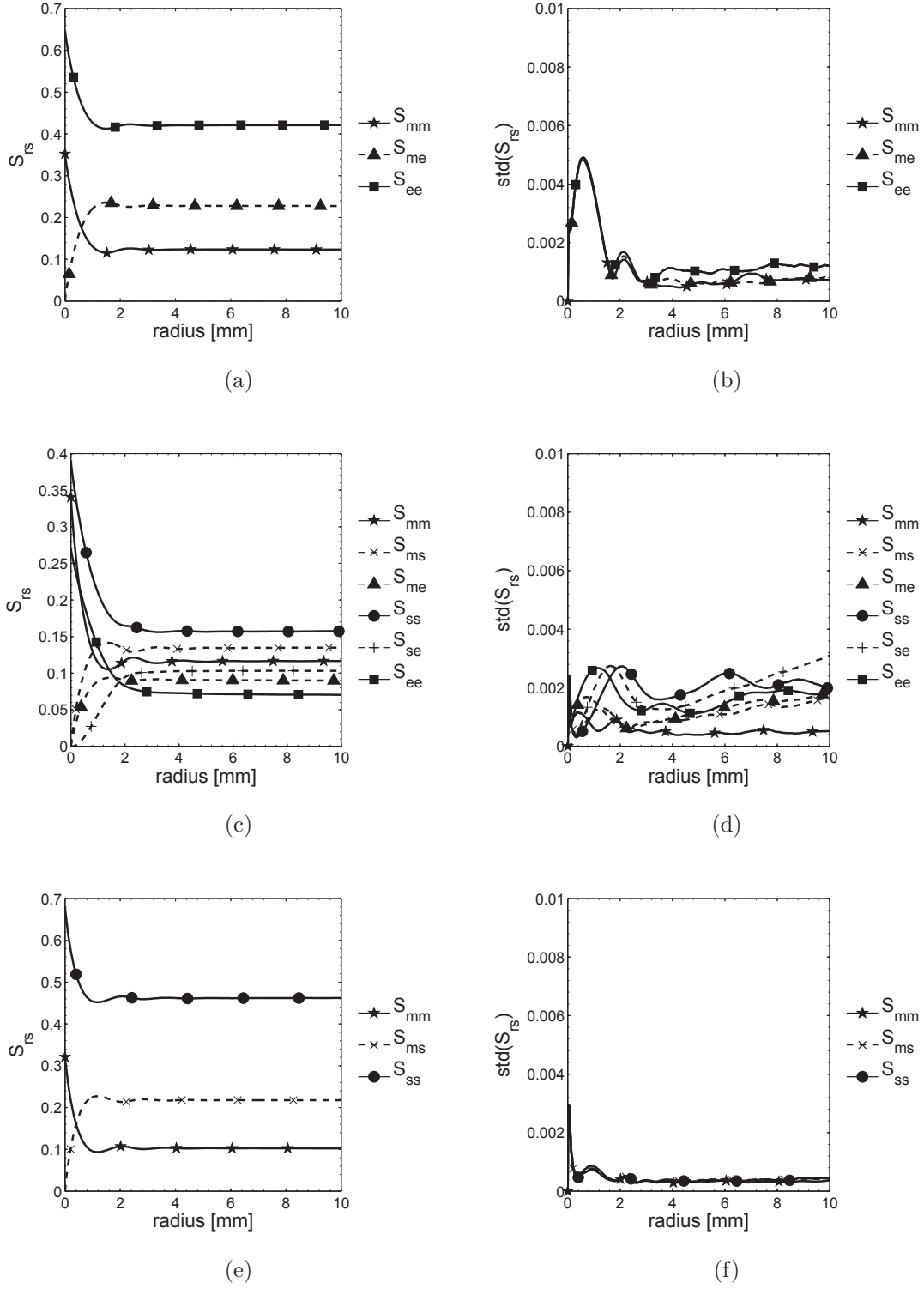
FIG. 18. Mean and standard deviations of two-point probability functions for randomized packs of 0% ((a)-(b)), 50% ((c)-(d)), and 100% ((e)-(f)) weight of spherical particles.

V. OVERALL ANISOTROPIC PROPERTY CALCULATIONS

In this work, it is assumed that the ellipsoidal particles exhibit transverse isotropic behavior ($\{\kappa_e^{\eta_1}, \kappa_e^{\eta_2}, \kappa_e^{\eta_3}\} = \{400, 100, 100\}$ W/mK), while the matrix and spherical particle phases are isotropic ($\kappa_m = 10$ W/mK, $\kappa_s = 50$ W/mK). A volume averaged conductivity tensor for the ellipsoidal phase is computed as

$$\boldsymbol{\kappa}_e(\boldsymbol{x}) = \frac{1}{\Omega_e} \int \boldsymbol{R}^T \boldsymbol{\kappa}_e^{\eta} \boldsymbol{R} \, \chi_e(\boldsymbol{x}) \mathrm{d}\Omega, \tag{23}$$

where $\boldsymbol{R}$ is the rotation matrix associated with the orientation of the particle, and χ_e is the indicator function for the ellipsoidal particles as defined in Equation (7). For an isotropic distribution of transverse isotropic ellipsoidal particles, the volume averaged tensor would be isotropic with the mean thermal conductivity $\kappa_e = 200$ W/mK. This was verified by considering uniformly distributed rotation matrices for the given transverse isotropic conductivity tensor [59]. However, for an anisotropic distribution of particles, the volume averaged tensor can lead to a symmetric anisotropic conductivity tensor.

As described in Section III B, the integrals present in Equations (16), (17) and (19) are integrated numerically using the adaptive sparse-grid Smolyak integration method with hierarchical basis. As discussed in [42], the numerical accuracy depends on three parameters, namely the quality of the interpolation defined as $\hat{\varepsilon}$, the quality of the integration defined as $\tilde{\varepsilon}$, and on the convergence of the integral, $\mathcal{E}_{\mathcal{I}}$. The quality of the interpolation, $\hat{\varepsilon}$, is the cutoff that determines which grid points remain in the sparse grid. We use $\hat{\varepsilon} = 1 \times 10^{-8}$ and 1×10^{-4} for the lower and upper bound calculations, respectively. The quality of the integration, $\tilde{\varepsilon}$, is related to the volume removed in the integral due to the singularity and is denoted as

$$\int_{\Omega_{\boldsymbol{x}'}} \boldsymbol{\Gamma}(\boldsymbol{x} - \boldsymbol{x}') \left(S_{rs}(\boldsymbol{x} - \boldsymbol{x}') - c_r c_s\right) \mathrm{d}\Omega_{\boldsymbol{x}'} \approx$$

$$\mathcal{I} = \int_{\Omega_{\boldsymbol{x}'}} \boldsymbol{\Gamma}_s \left(S_{rs}(\boldsymbol{x} - \boldsymbol{x}') - c_r c_s\right) \delta\left(\boldsymbol{x} - \boldsymbol{x}'\right) \mathrm{d}\Omega_{\boldsymbol{x}'} \tag{24}$$

$$+ \int_{\Omega_{\boldsymbol{x}'} \setminus v} \boldsymbol{\Gamma}_f(\boldsymbol{x} - \boldsymbol{x}') \left(S_{rs}(\boldsymbol{x} - \boldsymbol{x}') - c_r c_s\right) \mathrm{d}\Omega_{\boldsymbol{x}'}.$$

Here, $\boldsymbol{\Gamma}_s$ and $\boldsymbol{\Gamma}_f$ denote the singular and formal terms of $\boldsymbol{\Gamma}$, and a discussion on the derivation of these terms is provided in Appendix A. $\delta(\boldsymbol{x} - \boldsymbol{x}')$ is the Dirac delta function, and v is the small volume close to the singularity of $\boldsymbol{\Gamma}_f$ that we remove. This volume v is a sphere of

radius $\tilde{\varepsilon}$ removed around the origin ($\boldsymbol{x} = \boldsymbol{x}'$). After a convergence study, we selected $\tilde{\varepsilon} = 0.1$ mm for all computations. All solutions are stopped when the integrals converge within a certain tolerance,

$$\mathcal{E}_{\mathcal{I}} = |\mathcal{I}_h - \mathcal{I}_{h-1}|/|\mathcal{I}_{h-1}| \leq tol = 0.001, \tag{25}$$

where the subscript h is the sparse grid integration level (see [42] for more details). In order to quantify the overall numerical error due to the numerical parameters mentioned above, we define

$$e_n = \frac{||\overline{\boldsymbol{\kappa}}_{S_{rs}(|\boldsymbol{x}-\boldsymbol{x}'|)} - \overline{\boldsymbol{\kappa}}_s||_{\mathbb{F}}}{||\overline{\boldsymbol{\kappa}}_s||_{\mathbb{F}}} \times 100[\%]. \tag{26}$$

This definition takes advantage of the property of $\boldsymbol{\Gamma}_f$, where

$$\lim_{v \to 0} \int_{\Omega_{\boldsymbol{x}'} \backslash v} \boldsymbol{\Gamma}_f(\boldsymbol{x} - \boldsymbol{x}') f(\boldsymbol{x} - \boldsymbol{x}') \, \mathrm{d}\Omega_{\boldsymbol{x}'} = 0 \tag{27}$$

for any statistically isotropic function, $f(\boldsymbol{x} - \boldsymbol{x}')$. In Equation (26), $\overline{\boldsymbol{\kappa}}_{S_{rs}(|\boldsymbol{x}-\boldsymbol{x}'|)}$ is computed by numerically evaluating the integral $\mathcal{I}$ with isotropic statistics, and $\overline{\boldsymbol{\kappa}}_s$ is obtained in a closed form [28]. Considering the property in Equation (27), the overall numerical error in Equation (26) measures the accuracy of the numerical integration of the kernel including $\boldsymbol{\Gamma}_f$ (see Equation (24)). Note that $\overline{\boldsymbol{\kappa}}_{S_{rs}(|\boldsymbol{x}-\boldsymbol{x}'|)}$ is not a physically meaningful quantity and is only used to determine the numerical error of the calculations. All overall thermal conductivity tensor calculations presented hereafter are computed with a numerical error $e_n < 0.16\%$. Note that we are using the material characteristic length scale to integrate over $\Omega_{\boldsymbol{x}'}$ (see discussion in sections IV A and IV B), and a convergence study has been performed to verify the far limit of the integration.

When computing the self-consistent estimate, the NLOPT library [60] (nonlinear optimization package) was used for minimizing the objective functions (Equation (19)). For this work, the objective function is considered converged when the function value is less than 1×10^{-6}. Note that the objective function is approaching 0 as $\boldsymbol{\kappa}_0 \to \overline{\boldsymbol{\kappa}}$. It has been confirmed that the self-consistent estimates using both the upper and lower formulations of $\overline{\boldsymbol{\kappa}}$ (see Equation (19)) yield identical results. This is another verification test.

The resulting bounds and self consistent estimate of the overall anisotropic thermal conductivity tensor for the semi-ordered pack of ellipsoids are listed in Table III, where the eigenvalues of the overall conductivity tensor are presented. The eigenvalues of the conductivity tensor ($\overline{\kappa}_1$, $\overline{\kappa}_2$, and $\overline{\kappa}_3$) correspond to the components of the conductivity tensor

	$\overline{\kappa}_1$ [W/mK]	$\overline{\kappa}_2$ [W/mK]	$\overline{\kappa}_3$ [W/mK]	mean($\overline{\kappa}_1,\overline{\kappa}_2,\overline{\kappa}_3$)
	Isotropic distribution of particles			
$\overline{\boldsymbol{\kappa}}_i$ (LB)	————————————50.55————————————			
$\overline{\boldsymbol{\kappa}}_i$ (SC)	————————————108.85————————————			
$\overline{\boldsymbol{\kappa}}_i$ (UB)	————————————119.47————————————			
	Anisotropic model			
$\overline{\boldsymbol{\kappa}}_a$ (LB)	59.74	48.47	44.11	50.77
$\overline{\boldsymbol{\kappa}}_a$ (SC)	141.45	99.65	85.27	108.79
$\overline{\boldsymbol{\kappa}}_a$ (UB)	154.39	109.26	92.23	118.62

TABLE III. Overall thermal conductivity tensor predictions for semi-ordered pack.

in the principal coordinate frame, where the material behaves as an orthotropic one. $\overline{\boldsymbol{\kappa}}_i$ (subscript i stands for isotropic) refers to the assumption that the particles are isotropically distributed (perfectly random), with $\kappa_e = 200$ W/mK, leading to a macroscopically isotropic conductivity tensor with one independent component ($\overline{\kappa}_1 = \overline{\kappa}_2 = \overline{\kappa}_3$). $\overline{\boldsymbol{\kappa}}_i$ is calculated in a closed form. $\overline{\boldsymbol{\kappa}}_a$ is the anisotropic conductivity tensor (subscript a stands for anisotropic), which considers both the anisotropic constituent and statistically anisotropic configuration. $\overline{\boldsymbol{\kappa}}_a$ is calculated numerically.

As can be seen in Table III, the components of the anisotropic thermal conductivity tensor vary significantly. For example, in the upper bound of $\overline{\boldsymbol{\kappa}}_a$, the difference between the minimum and maximum eigenvalue is $154.39 - 92.23 = 62.16$ W/mK. For the lower bound of $\overline{\boldsymbol{\kappa}}_a$, we obtain $59.74 - 44.11 = 15.63$ W/mK. While the standard deviations in the statistical functions were moderate (see Figure 16), these deviations have a significant effect on the overall material behavior as they are magnified by the anisotropy in $\boldsymbol{\kappa}_e$ (see Equation (23)). Note that the mean of the eigenvalues of $\overline{\boldsymbol{\kappa}}_a$ is nearly identical to results for $\overline{\boldsymbol{\kappa}}_i$ for all three models (UB, LB and SC).

The resulting upper and lower bounds of the thermal conductivity tensor for the five randomized packs and the semi-ordered pack are presented in Figure 19. Here, $\overline{\kappa}^{max,min}$ refers to the maximum/minimum eigenvalues of the overall conductivity tensor. These maximum and minimum conductivity components (solid lines with triangles for LB and dashed lines with triangles for UB) are compared to those assuming an isotropic distribution of particles,
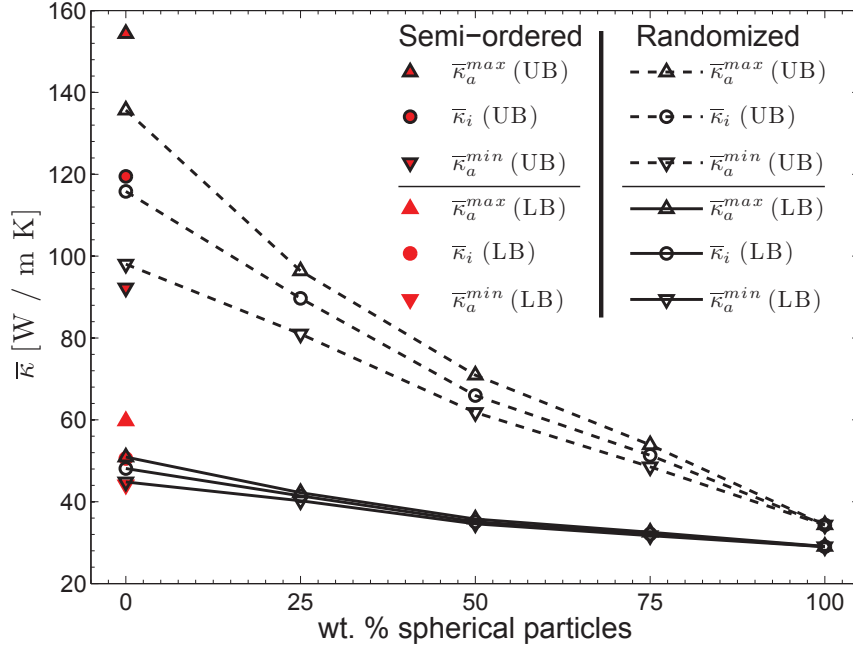
FIG. 19. Macroscopic bounds for anisotropic thermal conductivity of all compositions considered.

$\overline{\kappa}_i$ (solid line with circles for LB and dashed line with circles for UB). Note that $\overline{\kappa}_i$ (UB) and $\overline{\kappa}_i$ (LB) were computed with $\kappa_2 = 200$ W/mK. In general, the spread of the bounds increases for packs with more ellipsoidal particles, because the difference between the conductivities of an ellipsoidal particle and the matrix is larger than the difference between the conductivities of a sphere and the matrix (see lines with circles in Figure 19). Also note that the spread in the minimum and maximum components of $\overline{\boldsymbol{\kappa}}_a$ for both bounds increases for packs with more ellipsoidal particles due to the increasing amount of statistical anisotropy present in the packs. Recall that the statistical anisotropy was quantified based on the standard deviations in the two point probability functions (see Figure 18(b), (d), and (f)). The spread in the components of the conductivity tensor for the lower bound is smaller than the spread for the upper bound, since the least conductive constituent (matrix) is isotropic and the most conductive constituent (ellipsoids) is anisotropic.

When comparing the semi-ordered pack of ellipsoids (filled markers on left in Figure 19) to the randomized pack of ellipsoids, first note that the semi-ordered pack has a larger $\overline{\kappa}_i$ than the randomized pack, because the semi-ordered system has a higher packing fraction (see subsection II E 2). Also note that the spread of the conductivity components is larger

35

for the semi-ordered pack due to the larger statistical anisotropy present in the semi-ordered pack (compare Figures 18(b) and 16(b)). We will comment on the extent of these differences when we introduce a measure of anisotropy below.
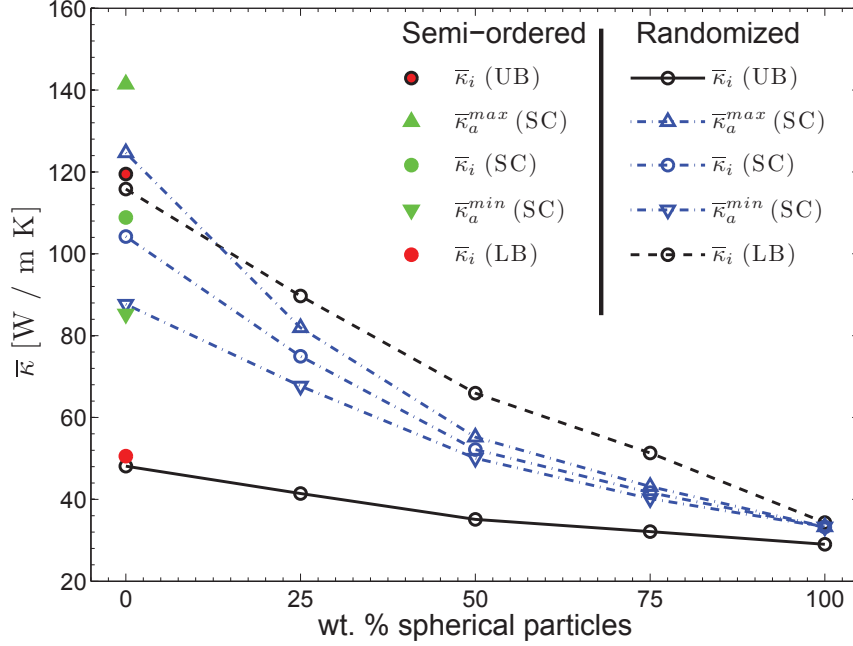

FIG. 20. Self-consistent estimates for anisotorpic thermal conductivity of all compositions considered.

The self-consistent estimates for the mixtures are presented in Figure 20. The same trends described for Figure 19 are observed. In order to compare the self-consistent estimates to the LB and UB computations, we also show the isotropic LB and UB behavior, respectively. Note that the self-consistent estimates are closer to the upper bound calculations, since this second-order model is strongly dependent on the volume fraction, and all of the packs have volume fractions greater than 0.6. Also note that there is no restriction on the self-consistent estimate being between the lower and upper bounds.

In order to quantify the macroscopic anisotropy of the thermal conductivity tensor, a measure of anisotropy, M_A, is defined as

$$M_A = \max(|\overline{\kappa}_a^{max} - \overline{\kappa}_i|, |\overline{\kappa}_a^{min} - \overline{\kappa}_i|)/\overline{\kappa}_i \times 100[\%]. \tag{28}$$

Computed measures of anisotropy for results in Figures 19 and 20 are presented in Figure 21. As alluded to above, the measure of anisotropy increases as more ellipsoidal particles are
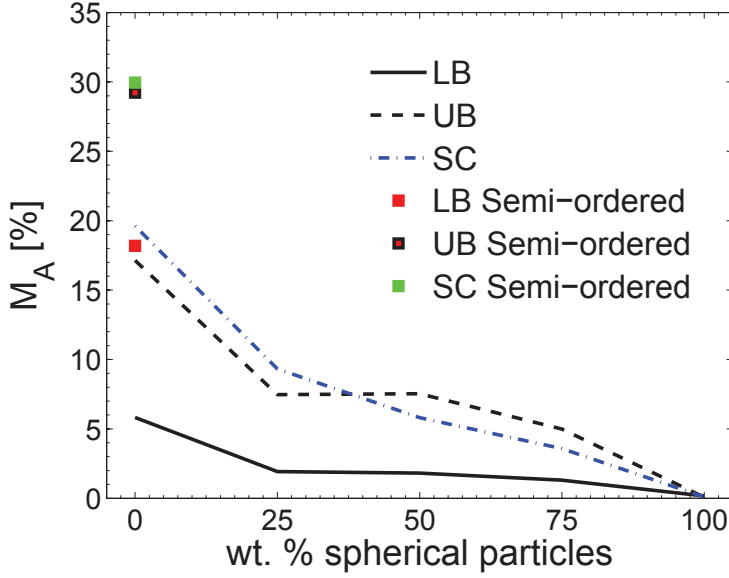
FIG. 21. Measure of anisotropy for all results.

present due to the increasing statistical anisotropy in the system. Let us consider the measure of anisotropy for the upper bound (dashed black line in Figure 21). Here $M_A = 0.08\%$ for the 100% mixture (all spheres) and increases up to $M_A = 17.14\%$ for the 0% mixture (all ellipsoids). For the lower bound, M_A grows from $M_A = 0.16\%$ to $M_A = 5.82\%$. The measures of anisotropy of the upper and lower bounds for the 100% mixture (all spheres) are near the numerical error, $|M_A(UB) - M_A(LB)| = 0.08\%$ ($e_n = 0.16\%$). Note that the anisotropic upper and lower bounds are rigorous bounds on the overall anisotropic thermal conductivity tensor. Therefore, these upper and lower bounds also provide limits on the measure of anisotropy. For example, the anisotropy of the 0% mixture (all ellipsoids) falls between $M_A = 5.82\%$ (LB) and $M_A = 17.14\%$ (UB).

The measures of anisotropy for the semi-ordered pack (filled markers in Figure 21) are significantly larger than the estimates of the randomized packs and are bounded between $M_A = 18.19\%$ (LB) and $M_A = 29.23\%$ (UB). Let us consider the upper bound results, where $M_A = 29.23\%$ for the semi-ordered pack (red filled square with black outline in Figure 21) as compared to $M_A = 17.14\%$ for the randomized pack of ellipsoids (dashed black line at 0% wt. spherical particles in Figure 21), and let us contrast those to $std(S_{rs}) = 0.0072$ for the semi-ordered pack and $std(S_{rs}) = 0.0049$ for the randomized pack (see section IV). Note that the measure of anisotropy for the self-consistent estimates of the 0% and 25%

37

mixtures (blue dotted dashed line) is higher than the anisotropy in the upper bound (black dashed line). Just as a self-consistent estimate is not guaranteed to be between the upper and lower bounds, the measure of anisotropy associated with this estimate is not expected to be between the upper and lower bounds.

VI.   CONCLUSIONS

In this work, we present a systematic microstructure characterization procedure anchored in micro-CT data that is used to establish microstructure-statistics-property relations of polydisperse particulate mixtures. A novel image processing pipeline is developed that accurately identified particles while maintaining low errors. Improvements in the image processing pipeline are achieved when compared to a traditional techniques. For all compositions considered, the volume losses due to image segmentation are less than 4%. These low errors indicate that scientifically sound and repeatable results have been achieved. Next, we developed a description of the polydisperse system in continuous Euclidean space. This idealized representation provides a substantial reduction in the dataset size and enables easier data manipulation and understanding.

After characterizing the microstructure, n-point probability functions of real polydisperse mixtures are calculated. We show that second-order probability functions do not exhibit ellipsoidal nor any other material symmetry. Therefore, assessment of overall material constants in a closed form is unattainable.

The statistical description is then used to compute bounds and self-consistent estimates of the anisotropic thermal conductivity tensor using the Hashin-Shtrikman variational principle. This is the first time to the best of our knowledge, that the anisotropic second-order estimates are calculated without assumptions on the inclusion's shape, configuration and/or material anisotropy. The overall properties show increasing anisotropy in the overall thermal conductivity tensor for packs with more transverse isotropic ellipsoidal inclusions. Moreover, the upper and lower bounds provide limits on the anisotropy of the mixtures. Due to the larger amounts of statistical anisotropy for the semi-ordered mixture, the measure of anisotropy for the overall conductivity tensor of this pack was significantly larger than for the randomized one.

VII.   ACKNOWLEDGMENTS

Appendix A: Discussion on $\Gamma(x, x')$

The infinite homogeneous Green's function for steady-state heat conduction of an anisotropic material is

$$g(\boldsymbol{x} - \boldsymbol{x}') = \frac{1}{(\mathsf{d} - 2)\Omega(\mathsf{d})R}\det\left(\boldsymbol{\kappa}^{-1}\right), \tag{A1}$$

where $\det(\bullet)$ stands for the determinant, $R = ((\boldsymbol{x} - \boldsymbol{x}') \cdot \boldsymbol{\kappa} \cdot (\boldsymbol{x} - \boldsymbol{x}'))^{1/2}$, $\mathsf{d} = 3$ is the dimension, and $\Omega(\mathsf{d})$ is the total solid angle in a d-dimensional sphere [61, 62]. Following the work of Torquato [63], $\boldsymbol{\Gamma}(\boldsymbol{x} - \boldsymbol{x}')$ is obtained by first considering a temperature field defined as

$$T(\boldsymbol{x}) = T_0(\boldsymbol{x}) - \int_{\Omega_{\boldsymbol{x}'}} \nabla g(\boldsymbol{x} - \boldsymbol{x}') \cdot \boldsymbol{p}(\boldsymbol{x}') \mathrm{d}\Omega. \tag{A2}$$

After integrating this equation by parts, using the Gauss-divergence theorem, and excluding a small spherical region around $\boldsymbol{x} = \boldsymbol{x}'$, one obtains

$$\boldsymbol{Q} = \boldsymbol{Q}_0 + \int_{\Omega_{\boldsymbol{x}'}} \boldsymbol{\Gamma}(\boldsymbol{x} - \boldsymbol{x}') \cdot \boldsymbol{p}(\boldsymbol{x}') \mathrm{d}\Omega. \tag{A3}$$

The resulting $\boldsymbol{\Gamma}(\boldsymbol{x} - \boldsymbol{x}')$ used in Equation (16) is defined as

$$\boldsymbol{\Gamma}(\boldsymbol{x} - \boldsymbol{x}') = \boldsymbol{\Gamma}_f(\boldsymbol{x} - \boldsymbol{x}') - \boldsymbol{\Gamma}_s\delta(\boldsymbol{x} - \boldsymbol{x}'), \tag{A4}$$

where

$$\boldsymbol{\Gamma}_s = \int_{|\boldsymbol{x} - \boldsymbol{x}'| = R_s} (g_{,i}\hat{n}_j + g_{,j}\hat{n}_i) \, \mathrm{d}\Omega \tag{A5}$$

and

$$\boldsymbol{\Gamma}_f(\boldsymbol{x} - \boldsymbol{x}') = \frac{\partial^2 g}{\partial x_i \partial x_j}. \tag{A6}$$

39

Here, the unit normal $\hat{\boldsymbol{n}}$ is the unit normal of the spherical surface ($|\boldsymbol{x} - \boldsymbol{x}'| = R_s$) over which the integration occurs. For an isotropic material, $\boldsymbol{\Gamma}_s$ can be integrated analytically, while obtaining an analytical solution becomes increasingly difficult for an anisotropic one. In this work, the singular term is computed numerically using an adaptive multi-dimensional integration scheme provided as an extension to the GNU Scientific Library (GSL). The singular term is calculated until the relative error of the integral is less than 1×10^{-5}. Note that the integral of $\boldsymbol{\Gamma}_f(\boldsymbol{x} - \boldsymbol{x}')$ over the surface of a sphere is zero,

$$\int_{|\boldsymbol{x} - \boldsymbol{x}'| = R_s} \boldsymbol{\Gamma}_f(\boldsymbol{x} - \boldsymbol{x}') \mathrm{d}\Omega = \boldsymbol{0}. \tag{A7}$$

[1] S. Kochevets, T. J. J. Buckmaster, and A. Hegab, Journal of Propellant and Power **17**, 883 (2001).

[2] K. Matouš, H. Inglis, X. Gu, D. Rypl, T. Jackson, and P. Geubelle, Composites Science and Technology **67**, 1694 (2007).

[3] J. Andrade and X. Tu, Mechanics of Materials **41**, 652 (2009).

[4] P. Chaikin and T. Lubensky, *Principles of Condensed Matter Physics* (Cambridge University Press, New York, 2000).

[5] J. Liang and K. Dill, Biophysical Journal **81**, 751 (2001).

[6] P. Breton, D. Ribereau, C. Marraud, and P. Lamarque, International Journal of Energetic Materials and Chemical Propulsion **5**, 132 (2002).

[7] J. Kepler, *Strena Seu de Niue Sexangula* (Godefridum Tampach, Francofurti ad Moenum, 1611) translated as J. Kepler, *The Six-Cornered Snowflake* (Clarendon, Oxford, 1966).

[8] T. C. Hales, Annals of Mathematics **162**, 1065 (2005).

[9] Y. Jiao, F. Stillinger, and S. Torquato, Physical Review E **79**, 041309 (2009).

[10] F. Maggi, S. Stafford, T. L. Jackson, and J. Buckmaster, Physical Review E **77**, 046107 (2008).

[11] X. Jia and R. Williams, Powder Technology **120**, 175 (2001).

[12] R. Caulkin, X. Jia, C. Xu, M. Fairweather, R. A. Williams, H. Stitt, M. Nijemeisland, S. Aferka, M. Crine, A. Leonard, D. Toye, and P. Marchot, Industrial & Engineering Chemistry Research **48**, 202 (2009).

[13] S. Gallier and F. Hiernard, Journal of Propulsion and Power **24**, 147 (2008).

[14] B. Collins, F. Maggi, K. Matouš, T. Jackson, and J. Buckmaster, in *46th AIAA Aerospace Sciences Meeting and Exhibit* (AIAA, 2008) paper No: AIAA 2008-941.

[15] T. Aste, M. Saadatfar, and T. Senden, Physical Review E **71**, 061302 (2005).

[16] H. Lee, M. Brandyberry, A. Tudor, and K. Matouš, Physical Review E **80**, 061301 (2009).

[17] C. Arns, M. Knackstedt, and W. Pinczewski, Geophysics **67**, 1396 (2002).

[18] J. Bernal, Nature **183**, 141 (1959).

[19] H. L. Frisch and F. H. Stillinger, Journal of Chemical Physics **38**, 2200 (1962).

[20] M. B. Weissman, Annual Review of Materials Science **26**, 395 (1996).

[21] J. Schmalzing and K. M. Grski, Monthly Notices of the Royal Astronomical Society **297**, 355 (1998).

[22] C. Coker and S. Torquato, Journal of Applied Physics **77**, 6087 (1995).

[23] C. Yeong and S. Torquato, Physical Review E **58**, 224 (1998).

[24] D. T. Fullwood, S. R. Niezgoda, and S. R. Kalidindi, Acta Materialia **56**, 942 (2008).

[25] G. T. Seidler, G. Martinez, L. H. Seeley, K. H. Kim, E. A. Behne, S. Zaranek, B. D. Chapman, S. M. Heald, and D. L. Brewe, Phys. Rev. E **62**, 8175 (2000).

[26] K. Mecke and C. H. Arns, Journal of Physics: Condensed Matter **17**, S503 (2005).

[27] Z. Hashin and S. Shtrikman, Journal of the Mechanics and Physics of Solids **10**, 335 (1962).

[28] J. Willis, Journal of the Mechanics and Physics of Solids **25**, 185 (1977).

[29] A. Bensoussan, J. Lions, and G. Papanicolaou, *Asymptotic Analysis for Periodic Structures.* (New York: North-Holland, 1978).

[30] R. Hill, Math. Proc. Camb. Phil. Soc. **98**, 579 (1985).

[31] S. Torquato, Physical Review Letters **79**, 681 (1997).

[32] R. Christensen and K. Lo, Journal of the Mechanics and Physics of Solids **27**, 315 (1979).

[33] G. Dvorak and M. Srinivas, Journal of the Mechanics and Physics of Solids **47**, 899 (1999).

[34] D. Fullwood, B. Adams, and S. Kalidindi, Journal of the Mechanics and Physics of Solids **56**, 2287 (2008).

[35] L. Walpole, Journal of the Mechanics and Physics of Solids **14**, 151 (1966).

[36] P. Areias and K. Matouš, Computer Methods in Applied Mechanics and Engineering **197**, 4702 (2008).

[37] C. Yeong and S. Torquato, Physical Review E **57**, 495 (1998).

[38] W. Drugan and J. Willis, Journal of the Mechanics and Physics of Solids **44**, 492 (1996).

[39] S. Torquato and A. K. Sen, Journal of Applied Physics **67**, 1145 (1990).

[40] P. Castaneda, Physical Review B **57**, 12077 (1998).

[41] D. Talbot and J. Willis, Journal of the Mechanics and Physics of Solids **45**, 87 (1997).

[42] H. Lee, A. Gillman, and K. Matouš, Journal of the Mechanics and Physics of Solids **56(10)**, 1838 (2011).

[43] J. Baker and A. Kudrolli, Phys. Rev. E **82**, 061304 (2010).

[44] G. D. Scott and D. M. Kilgour, Journal of Physics D: Applied Physics **2**, 863 (1969).

[45] J. Russ, *The Image Processing Handbook*, Image Processing Handbook (Taylor & Francis, 2006).

[46] V. I. Inc., "Amira," `http://www.amira.com/`.

[47] B. microCT, "Skyscan: Microtomography, nanotomography, non-invasive 3d xray microscopy," `http://www.skyscan.be/home.htm`.

[48] K. Preston and M. Onoe, *Digital processing of biomedical images* (Plenum Press, 1976).

[49] G. Windreich, N. Kiryati, and G. Lohmann, Pattern Recognition **36**, 2531 (2003).

[50] J. Lindblad, Image and Vision Computing **23**, 111 (2005).

[51] P. M. Chaikin, A. Donev, W. Man, F. H. Stillinger, and S. Torquato, Industrial & Engineering Chemistry Research **45**, 6960 (2006).

[52] R. K. McGEARY, Journal of the American Ceramic Society **44**, 513 (1961).

[53] A. Donev, F. H. Stillinger, P. M. Chaikin, and S. Torquato, Phys. Rev. Lett. **92**, 255506 (2004).

[54] A. Donev, R. Connelly, F. H. Stillinger, and S. Torquato, Phys. Rev. E **75**, 051304 (2007).

[55] S. Torquato, *Random Heterogeneous Materials* (Springer, New York, 2002).

[56] M. Beran, *Statistical Continuum Theories* (Interscience Publishers, 1968).

[57] L. Onsager, Phys. Rev. **37**, 405 (1931).

[58] G. Weng, International Journal of Engineering Science **30**, 83 (1992).

[59] J. Arvo (Academic Press Professional, Inc., San Diego, CA, USA, 1992) Chap. Fast random rotation matrices, pp. 117–120.

[60] S. G. Johnson, "The nlopt nonlinear-optimization package," `http://ab-initio.mit.edu/nlopt`.

[61] H.-Y. Kuo and T. Chen, International Journal of Solids and Structures **42**, 1111 (2005).

[62] Y. Chang, C. Kang, and D. J. Chen, International Journal of Heat and Mass Transfer **16**, 1905 (1973).

[63] S. Torquato, Journal of the Mechanics and Physics of Solids **45**, 1421 (1997).